

# Comparison of REV size and tensor characteristics for the electrical and hydraulic conductivities in fractured rock

Serdar Demirel<sup>1</sup>, James Irving<sup>1\*</sup>, and Delphine Roubinet<sup>2</sup>

<sup>1</sup> Institute of Earth Sciences, University of Lausanne, Switzerland

<sup>2</sup> Geosciences Montpellier (CNRS), University of Montpellier, France

\* Corresponding author (james.irving@unil.ch)

Revised draft for *Geophysical Journal International*

Abbreviated title: Comparison of REV size and tensor characteristics

## 1 **Summary**

2 The representative elementary volume (REV) is a critically important concept in fractured  
3 rock investigations as it tells us at what scale the fractured domain can be represented by an  
4 anisotropic tensor as opposed to requiring the details of each individual fracture for modeling  
5 purposes. Whereas the REV size and corresponding tensor characteristics for the hydraulic  
6 conductivity ( $K$ ) in fractured rock have been the subject of numerous previous investigations,  
7 no studies to date have focused on the electrical conductivity ( $\sigma$ ). This is despite the fact  
8 that geoelectrical measurements are arguably the most popular means of geophysically in-  
9 vestigating fractured rock, typically via azimuthal resistivity surveying where the observed  
10 electrical anisotropy is commonly used to infer hydraulic characteristics. In this paper, we  
11 attempt to fill this void and present a systematic numerical study of the impacts of changes  
12 in fracture-network properties on the REV size and equivalent tensor characteristics for both  
13 the electrical and hydraulic conductivities. We employ a combined statistical and numerical  
14 approach where the size of the REV is estimated from the conductivity variability observed  
15 across multiple stochastic fracture-network realizations for various domain sizes. Two im-  
16 portant differences between fluid and electric current flow in fractured media are found to

17 lead to significant differences in the REV size and tensor characteristics for  $\sigma$  and  $K$ ; these  
18 are the greater importance of the matrix in the electrical case and the single-power instead  
19 of cubic dependence of electric current flow upon aperture. Specifically, the REV for the  
20 electrical conductivity will always be smaller than that for the hydraulic conductivity, and  
21 the corresponding equivalent tensor will exhibit less anisotropy, often with notably different  
22 principal orientations. These findings are of key importance for the eventual interpretation of  
23 geoelectrical measurements in fractured rock, where we conclude that extreme caution must  
24 be taken when attempting to make the link to hydraulic properties.

25 *Keywords:* electrical conductivity; hydraulic conductivity; representative elementary volume  
26 (REV); representative volume element (RVE); tensor; discrete-dual-porosity (DDP); discrete  
27 fracture network (DFN); resistivity; stochastic; geoelectrical

## 28 **1 Introduction**

29 Fractured rocks play a critically important role in a wide variety of geoscience problems  
30 including groundwater flow and contaminant transport, aquifer remediation, hydrocarbon ex-  
31 traction, geothermal resource exploitation, and the long-term underground storage of CO<sub>2</sub>  
32 and nuclear waste (Carneiro, 2009; Follin et al., 2014; Geiger & Emmanuel, 2010; Kolditz  
33 & Clauser, 1998; Manna et al., 2017; Neuman, 2005; Rotter et al., 2008; Zhao et al., 2017).  
34 Numerous studies have been devoted to the development of methods for the identification  
35 and characterization of subsurface fractures and fracture networks, with the overall aim of  
36 improving conceptual and numerical models of flow and transport in fractured-rock environ-  
37 ments (Berkowitz, 2002; Bonnet et al., 2001; Davy et al., 2010; NAP, 2015). In this regard,  
38 applied geophysical methods have gained widespread interest, as many of these methods are  
39 highly sensitive to the presence of fractures and the corresponding measurements can be ac-  
40 quired quickly and non-invasively from the Earth’s surface and/or from boreholes. Examples  
41 include ground-penetrating radar (Dorn et al., 2012; Tsofiias et al., 2001), seismic (Her-  
42 wanger et al., 2004a; Pytharouli et al., 2011), electrical resistivity (Lane et al., 1995; Robert  
43 et al., 2012), induced polarization (Marescot et al., 2008; Schmutz et al., 2011), self potential

44 (DesRoches et al., 2017; Roubinet et al., 2016; Wishart et al., 2008), and electromagnetic  
45 methods (Donadille & Al-Ofi, 2012; Steelman et al., 2015).

46 Amongst the multitude of geophysical techniques that have been applied to fractured-rock  
47 problems, the electrical resistivity (ER) method is of particular interest because: (i) numerous  
48 field, laboratory, and theoretical studies have demonstrated that geoelectrical data are signif-  
49 icantly affected by the presence and characteristics of fractures such as density, orientation,  
50 and aperture (Jinsong et al., 2009; Taylor & Fleming, 1988); (ii) ER measurements can be ac-  
51 quired using a variety of electrode configurations and spacings, thereby offering the potential  
52 to obtain information on subsurface properties over a wide range of spatial scales (Everett,  
53 2013; Telford et al., 1990); and (iii) strong analogies between fluid and electric current flow in  
54 fractured media suggest that geoelectrical data may contain important information regarding  
55 the corresponding hydrogeological properties (Brown, 1989; Van Sicle, 2002). As a result,  
56 ER studies in fractured rock have been widespread, and include the development and applica-  
57 tion of anisotropic tomographic methods (Greenhalgh et al., 2009; Herwanger et al., 2004a,b;  
58 Li & Spitzer, 2005; Pain et al., 2003); the use of azimuthal resistivity surveys to estimate  
59 predominant fracture orientations (Al Hagrey, 1994; Busby, 2000; Lane et al., 1995; Taylor  
60 & Fleming, 1988) along with, in many cases, properties of the hydraulic conductivity tensor  
61 (Boadu et al., 2005, 2008; Ritzi & Andolsek, 1992; Skinner & Heinson, 2004; Skjærnaa &  
62 Jørgensen, 1994; Steinich & Marin, 1996; Yeboah-Forson & Whitman, 2014); and the acqui-  
63 sition of surface-based electrical resistivity tomography (ERT) profiles for the identification  
64 and characterization of fracture zones (Porsani et al., 2005; Robert et al., 2011, 2012; Sharma  
65 & Baranwal, 2005; Yadav & Singh, 2007).

66 One concept that is absolutely critical when it comes to making meaningful use of geoelec-  
67 trical data in fractured-rock investigations is the representative elementary volume (REV).  
68 In materials engineering, the REV is typically defined as the minimum volume of heteroge-  
69 neous material that is large enough to be statistically representative of the composite with  
70 respect to a particular physical property (Kanit et al., 2003). In other words, at volume sizes  
71 greater than the REV, small-scale heterogeneities in the medium need not be explicitly taken  
72 into account because their effects can be adequately captured by a set of average continuum

73 properties. With regard to geoelectrical measurements in fractured rock, the REV defines  
74 the scale beyond which the electrical conductivity of the fractured medium can be adequately  
75 described using a second-order tensor, thus avoiding the need to consider the detailed ef-  
76 fects of individual fractures on the passage of electric current. Knowledge about the REV is  
77 essential for understanding under what circumstances ERT forward modeling and inversion  
78 codes, which are based upon a discretized parameterization of the conductivity, can be ef-  
79 fectively utilized. Indeed, such codes inherently assume that the chosen model-cell size is at  
80 or beyond the scale at which conductivity can be effectively described by a scalar or tensor,  
81 which may or may not be valid. The notion of REV is also fundamental for understanding  
82 when and how bulk electrical properties can be related to those of the underlying fracture  
83 network (i.e., fracture densities, orientations, lengths, and apertures). Finally, it is essential  
84 to understand the nature of the REV for the electrical conductivity in fractured rock, and its  
85 relationship to the REV for the hydraulic conductivity, before conclusions can be made about  
86 subsurface hydrogeological properties based on geoelectrical measurements. As noted above,  
87 a number of researchers have taken the step of linking the results of azimuthal resistivity  
88 surveying to properties of the hydraulic conductivity tensor, with the justification that fluid  
89 and electric current will take similar paths through the fractured medium based on parallels  
90 between Ohm's and Darcy's laws. No study to date, however, has ever critically examined  
91 the validity of this approach in the context of realistic fracture networks.

92 Within the hydrogeological community, the existence and properties of the REV for the  
93 hydraulic conductivity in fractured rock have been rather extensively investigated. Snow  
94 (1969) conducted an analytical study in which he derived the anisotropic permeability tensor  
95 for fractured media assuming sets of infinitely long parallel fractures having different ori-  
96 entations, apertures, and spacings. Using a 2D discrete-fracture-network (DFN) numerical  
97 modeling approach and assuming an impermeable matrix, Long et al. (1982) subsequently  
98 investigated the REV size and permeability tensor characteristics for a variety of fracture  
99 networks, where fracture positions, orientations, lengths, and apertures were drawn randomly  
100 from statistical distributions. More recent research has continued along these lines, examining  
101 through numerical DFN simulations how the REV size and permeability tensor are affected

102 by the statistical distribution of fracture parameters (Min et al., 2004; Wang & Kulatilake,  
103 2008) as well as correlations between parameters (Baghbanan & Jing, 2007). With respect to  
104 the electrical conductivity, on the other hand, there is a near complete lack of information in  
105 the literature on the existence and properties of an REV in fractured rock. While the effects of  
106 fractures on the equivalent conductivity beyond the REV scale have been examined for simple  
107 configurations (Berryman & Hoversten, 2013; Jinsong et al., 2009), no studies have attempted  
108 to quantify the REV size and conductivity tensor characteristics for realistic fracture networks.  
109 The primary reason for this has been the absence of tools for numerically modeling electric  
110 current flow in fractured media. Whereas fluid flow can be rather easily examined because  
111 the rock matrix is often ignored on the basis that it is effectively impervious (Cvetkovic, 2017;  
112 Maillot et al., 2016; Neuman, 2005), this is not the case for the electrical conductivity where  
113 the matrix typically plays an important role in the conduction of electric current (Beskardes  
114 & Weiss, 2018; Caballero Sanz et al., 2017; Roubinet & Irving, 2014; Roubinet et al., 2016).  
115 As a result, modeling approaches that explicitly account for both the fractures and matrix, as  
116 well as interactions between these domains, are required. Unfortunately the use of standard  
117 numerical methods, for example finite-difference, -element, or -volume techniques where the  
118 fractures and matrix are fully discretized (Dey & Morrison, 1979; Pidlisecky & Knight, 2008;  
119 R ucker et al., 2006), has not been computationally feasible in this regard due to the extremely  
120 high number of model elements involved.

121 Recently, Roubinet & Irving (2014) presented a novel numerical modeling approach for  
122 electric current flow in 2D fractured media that is based on a semi-analytical discrete-dual-  
123 porosity formulation. For the first time, this methodology permits accurate computation of  
124 current flow through realistic and highly complex fracture networks with orders of magnitude  
125 less computational cost than standard numerical methods. Our goal in the current paper is  
126 to use this modeling approach to examine the REV size and tensor characteristics for the  
127 electrical conductivity in realistic fractured media, and to compare our findings with the cor-  
128 responding results obtained for the hydraulic conductivity. This is done in full generality with  
129 respect to the 2D intrinsic equivalent medium properties, and not in the context of a partic-  
130 ular field configuration or measurement setup. We examine the effects of changing fracture

131 orientations, apertures, and lengths, as well as imposing statistical correlation between aper-  
132 ture and length. In Section 2 we present the overall methodology behind our approach, which  
133 involves (i) the stochastic generation of 2D square DFNs for various domain sizes; (ii) running  
134 fluid and electric current flow simulations; (iii) determination of the mean and variance of the  
135 estimated 2D conductivity tensor components as a function of domain size; and (iv) estima-  
136 tion of the average tensorial properties of the medium and the REV size. An advantage of the  
137 combined numerical and statistical approach to REV estimation considered in this paper is  
138 that numerical simulations need not be performed at the REV scale in order to estimate the  
139 REV size. We then show in Section 3 the results of applying this procedure to 16 different  
140 test cases, which allows us to draw conclusions about how the REVs for the electrical and  
141 hydraulic conductivity compare and are affected by changes in the fracture distribution. This  
142 leads to some general discussion regarding the validity of inferring characteristics of the hy-  
143 draulic conductivity tensor from geoelectrical measurements, as well as implications for field  
144 measurements (Section 4).

## 145 **2 Methodology**

146 We use the combined numerical and statistical approach developed in Cailletaud et al. (1994)  
147 and Kanit et al. (2003) for our REV analysis, whereby the variance of the property of interest,  
148 quantified through the analysis of multiple stochastic realizations over several domain sizes,  
149 is used to establish a scaling relationship that permits definition of the REV in terms of a  
150 prescribed level of error. To this end, we generate random DFN realizations for different  
151 domain sizes based on chosen probability distributions for the fracture positions, orientations,  
152 lengths, and apertures. Numerical modeling of flow through the DFNs for two orthogonal  
153 sets of Dirichlet boundary conditions then allows estimation of the conductivity tensor com-  
154 ponents, whose mean values are used to determine the equivalent tensorial properties of the  
155 medium at and beyond the REV scale, and whose variability as a function of domain size is  
156 used to derive the scaling relationship required to estimate the size of the REV.

157 In accordance with previous work (Long et al., 1982; Min et al., 2004; Baghbanan &  
158 Jing, 2007), we conduct our analysis in 2D in this paper. This has the strong advantages of

159 (i) being orders of magnitude more computationally efficient than a 3D analysis while at the  
160 same time allowing for meaningful general conclusions to be made; and (ii) permitting use of  
161 the modeling framework of Roubinet & Irving (2014) for the electric current flow problem,  
162 with no further developments required. Fractures in the 2D DFNs are represented as 1D  
163 linear elements having a constant aperture along their length, and are assumed to be filled  
164 with water. Although the latter is clearly a gross simplification of reality in the sense that  
165 is it well known that (i) aperture varies within fractures; (ii) fracture walls are rough; and  
166 (iii) fracture filling/alteration is common (Brown, 1989; Van Sice, 2002), the aim of this  
167 study is to focus on the effects of the fracture-network rather than on details of the individual  
168 fractures. Indeed, all previous REV work has represented fractures using this simple parallel-  
169 plate model. The various steps involved in our analysis are described in detail below.

## 170 **2.1 DFN generation**

171 Fractures in this study are completely described by their center position, orientation, length,  
172 and aperture, for which we define probability distributions in order to generate a large number  
173 of stochastic DFN realizations. To create one of such realizations for a particular domain size,  
174 we populate an initial large-scale ( $100 \times 100$  m) region with fractures, from which a central  
175 square sub-domain having the desired side length  $L$  is extracted (Figure 1a and 1b). Fracture  
176 centers are assumed to be uniformly distributed in the  $x$  and  $y$  directions throughout the  
177 domain (Li et al., 2009; Li & Zhang, 2010; Wang & Kulatilake, 2008), meaning that the  
178 center point  $(x_c, y_c)$  of each fracture can be obtained by drawing  $x_c$  and  $y_c$  from  $\mathcal{U}[0, 100]$ .  
179 We consider a density of fracture centers of  $2 \text{ m}^{-2}$  for all of the examples considered in this  
180 paper, which is comparable with previous research efforts based on the analysis of fractures  
181 in the field (Baghbanan & Jing, 2007; Min et al., 2004; Wang & Kulatilake, 2008) and leads  
182 to the generation of 20,000 fractures in the  $100 \times 100$  m region. The latter parameter was not  
183 varied in our study as it is already well understood and rather intuitive that increasing the  
184 fracture density will tend to proportionally decrease the REV size and increase the overall  
185 magnitude of the domain conductivity (Li et al., 2009; Li & Zhang, 2010; Long et al., 1982;  
186 Wang & Kulatilake, 2008). Further, the fracture density value chosen in this paper is not

187 expected to have an impact on the general findings and conclusions in Section 3.

188 [Figure 1 about here.]

189 Two fracture sets having different orientations are considered in each of the test cases  
190 examined in Section 3 (Li et al., 2009; Long et al., 1982; Wang & Kulatilake, 2008). The  
191 fractures in the domain are distributed evenly between these two sets, and the orientation  
192 angles of fractures within each set are described by a normal distribution with mean  $\mu_\theta$  and  
193 standard deviation  $\sigma_\theta$ . Although other statistical distributions have been considered to model  
194 fracture orientations in previous REV studies (Baghbanan & Jing, 2007; Min et al., 2004),  
195 the normal distribution is the most common and straightforward choice (Li et al., 2009; Li &  
196 Zhang, 2010; Long et al., 1982; Wang & Kulatilake, 2008).

197 Fracture lengths are assumed to follow a power-law distribution, truncated at the lower  
198 end, whose probability density function (PDF) is given by

$$199 \quad f(\ell) = \begin{cases} k\ell^{-a} & \text{for } \ell \geq \ell_{min} \\ 0 & \text{otherwise} \end{cases}, \quad (1)$$

200

201 where  $\ell_{min}$  is the minimum permitted fracture length,  $a$  is the power-law exponent, and  $k$  is  
202 a normalization constant that ensures that the PDF integrates to unity. Use of a power-law  
203 distribution is arguably the most common means of describing fracture lengths in recent lit-  
204 erature (Baghbanan & Jing, 2007; de Dreuzy et al., 2001; Min et al., 2004), and is supported  
205 by a substantial volume of work on the analysis of fracture traces observed at the Earth's  
206 surface as well as theoretical studies (Bonnet et al., 2001; Bour & Davy, 1997; Davy et al.,  
207 2010). The latter research showed that the exponent  $a$  typically ranges between 1 and 3, with  
208 higher values corresponding to fracture networks dominated by short fractures and lower val-  
209 ues describing networks where the connectivity is controlled by longer fractures. To generate  
210 random values for  $\ell$  consistent with equation (1), we derive the associated cumulative dis-  
211 tribution function (CDF) and use the inverse transform sampling approach (Devroye, 1986).



212 The simulated value for the fracture length is obtained using

$$213 \quad \ell = \ell_{min} X^{\frac{1}{1-a}}, \quad (2)$$

214

215 where  $X$  is a uniform random number drawn from  $\mathcal{U}[0, 1]$ .

216 Finally, fracture apertures in our study are assumed to be either constant within each  
 217 fracture set (Min et al., 2004; Wang & Kulatilake, 2008) or randomly distributed according  
 218 to a truncated lognormal distribution (Baghbanan & Jing, 2007; Li et al., 2009; Li & Zhang,  
 219 2010; Long et al., 1982). The latter PDF is given by

$$220 \quad f(b) = \begin{cases} k \exp\left(-\frac{(\ln b - \mu_{\ln b})^2}{2\sigma_{\ln b}^2}\right) & \text{for } b_{min} \leq b \leq b_{max} \\ 0 & \text{otherwise} \end{cases}, \quad (3)$$

221

222 where  $b_{min}$  and  $b_{max}$  are the minimum and maximum permitted aperture values,  $\mu_{\ln b}$  and  $\sigma_{\ln b}$   
 223 are the mean and standard deviation of the natural logarithm of the aperture, and  $k$  is again  
 224 a normalization constant. As before, the inverse transform sampling approach can be used  
 225 with the corresponding CDF to generate random aperture values according to equation (3).  
 226 The simulated values are obtained using (Baghbanan & Jing, 2007)

$$227 \quad b = \exp\left(\sqrt{2}\sigma_{\ln b} \operatorname{erf}^{-1}\{X \cdot (g(b_{max}) - g(b_{min})) + g(b_{min})\} + \mu_{\ln b}\right), \quad (4)$$

228

229 where  $X$  is again a random number drawn from  $\mathcal{U}[0, 1]$ ,  $\operatorname{erf}^{-1}$  is the inverse error function,  
 230 and  $g(b) = \operatorname{erf}\{(\ln b - \mu_{\ln b})/\sqrt{2}\sigma_{\ln b}\}$  with  $\operatorname{erf}$  the error function. Note that a wide body of  
 231 research indicates that fracture aperture tends to be positively correlated with length (Bonnet  
 232 et al., 2001; Hatton et al., 1994; Klimczak et al., 2010; Neuman, 2008; Olson, 2003; Renshaw &  
 233 Park, 1997; Vermilye & Scholz, 1995). To simulate values from the probability distributions in  
 234 equations (1) and (3) while taking into account correlation between these variables, we simply  
 235 use the same uniform random deviate  $X$  to generate both values in equations (2) and (4),  
 236 respectively (Baghbanan & Jing, 2007). Also note that values for the parameters controlling  
 237 the fracture aperture distribution were chosen in our study to yield apertures within the

238 range of those “typically” encountered in fractured-rock environments (Lapcevic et al., 1997;  
239 Singhal & Gupta, 2010).

## 240 **2.2 Fluid flow model**

241 To compute fluid flow through the different DFN realizations, we follow previous work and  
242 assume that the rock matrix can be effectively treated as impervious on the basis that its  
243 ability to transmit fluid is typically many orders of magnitude less than that of the fracture  
244 network (Cacas et al., 1990; Long et al., 1982; NAP, 2015). In this case, consideration of  
245 steady-state laminar flow of an incompressible fluid through a 1D parallel-plate smooth-walled  
246 fracture leads to the so-called cubic law for the fracture transmissivity  $T$  [ $\text{m}^2 \text{s}^{-1}$ ] (Snow, 1969).

$$247 \quad T = \frac{\rho g}{12\mu} b^3, \quad (5)$$

248

249 where  $g$  is the acceleration of gravity [ $\text{m s}^{-2}$ ],  $\rho$  and  $\mu$  are the density [ $\text{kg m}^{-3}$ ] and dynamic  
250 viscosity [ $\text{kg m}^{-1} \text{s}^{-1}$ ] of the fluid, respectively, and  $b$  is the fracture aperture. To conduct  
251 our simulations, the DFN is first divided into fracture segments whose endpoints are formed  
252 by either (i) intersections between fractures and the domain boundaries; (ii) intersections  
253 between fractures themselves; or (iii) fracture extremities. The flow of water through each  
254 fracture segment is constant and determined solely by the product of the transmissivity and  
255 the negative hydraulic gradient, the latter of which is linear and given by the difference in  
256 hydraulic head between the segment endpoints divided by the length of the segment. This  
257 version of Darcy’s law, combined with the principle of mass conservation at each fracture  
258 intersection, are used to construct a linear system whose unknowns are the values of the  
259 hydraulic head at the fracture intersections (de Dreuzy et al., 2001; Gisladdottir et al., 2016;  
260 Long et al., 1982). Taking into account the boundary conditions imposed on the domain  
261 borders, we solve the linear system and use the resulting hydraulic head values to determine  
262 the flow through each of the fractures.

### 263 **2.3 Electric current flow model**

264 Computing the flow of electric current through the DFN realizations is significantly more  
265 complicated than the fluid-flow problem because the contribution of the rock matrix cannot  
266 be ignored. Indeed, the smaller contrast in conductivity between the fractures and matrix  
267 in this case means that we must not only account for current flow through the matrix, but  
268 also between the fractures and matrix, in addition to the current flow through the fracture  
269 network. To this end, we use the discrete-dual-porosity approach of Roubinet & Irving (2014)  
270 and refer the reader to this paper for details beyond the brief description given here. The  
271 equation that forms the basis for this approach, obtained by combining Ohm’s law with the  
272 principle of conservation of electric charge at the point scale, is the following:

$$273 \quad -\nabla \cdot (\sigma \nabla V) = Q, \quad (6)$$

274

275 where  $\sigma$  is the electrical conductivity [ $\text{S m}^{-1}$ ],  $V$  is the electric potential [V], and  $Q$  is a source  
276 (positive) or sink (negative) term [ $\text{C m}^{-3} \text{s}^{-1}$ ] that is used to account for charge movement  
277 between the fractures and matrix based on differences in their potential values.

278 To conduct the simulations, the matrix domain is divided into blocks at a chosen level  
279 of discretization and the DFN is again divided into fracture segments. This time, however,  
280 fracture-segment endpoints are defined by intersections between fractures and matrix-block  
281 boundaries in addition to the criteria given in Section 2.2. At the fracture-segment scale,  
282 equation (6) is used to derive an analytical expression for the 1D electric potential distribution  
283 along a segment, which depends on the potential values at the segment endpoints as well as  
284 on the potential value of the surrounding matrix block. In the simplified case of an insulating  
285 (zero conductivity) matrix, this expression reduces to a linear variation in potential between  
286 the endpoints, meaning that the electric current flow through the fracture can be obtained  
287 by multiplying the negative potential gradient with the electrical conductance  $G$  [S] of the  
288 fracture, given by:

$$289 \quad G = \sigma_f b, \quad (7)$$

290

291 where  $\sigma_f$  is the fracture electrical conductivity. We shall see later that this fundamental dif-  
 292 ference between electric current and fluid flow in an isolated fracture, namely the dependence  
 293 of flow rate on aperture to the first power for electric current (equation (7)) versus aperture  
 294 to the third power for fluid flow (equation (5)), contributes to significant differences between  
 295 the REV size and tensor characteristics for the electrical and hydraulic conductivities.

296 Similar to the fluid-flow case, the analytical expression for the electric potential along a  
 297 fracture segment is combined with the principle of charge conservation at the fracture-segment  
 298 junctions in order to construct a linear system. This system, which has more unknowns  
 299 than equations due to the addition of the unknown potential values of the matrix blocks,  
 300 is completed through the consideration of equation (6) at the matrix-block scale using a  
 301 finite-volume-type approach. Taking into account the boundary conditions imposed on the  
 302 domain borders, we solve the full linear system for the potential values at the fracture-segment  
 303 endpoints and in the matrix blocks, which allows us to compute the flow of electric current  
 304 through the fractured region.

## 305 **2.4 Estimation of 2D conductivity tensor components**

306 To estimate the hydraulic and electrical conductivity tensor components corresponding to  
 307 a particular DFN realization using the numerical models for fluid and electric current flow  
 308 described above, we consider two orthogonal sets of Dirichlet boundary conditions having  
 309 different fixed potential values on one set of opposing sides and a linear variation between  
 310 these values on the other sides (Baghbanan & Jing, 2007; Long et al., 1982; Min et al., 2004).  
 311 These boundary conditions, illustrated in Figure 1c and 1d, have the effect of creating a linear  
 312 potential gradient across the domain in the  $x$  and  $y$  directions, respectively. Assuming that  
 313 the conductivity in the 2D domain can be represented by a second-order tensor, the resulting  
 314 flux is given by

$$315 \quad \mathbf{q} = -\mathbf{C} \nabla \phi, \quad (8)$$

316

317 where  $\mathbf{q}$  is the flux vector (either  $[\text{m s}^{-1}]$  or  $[\text{C m}^{-2}\text{s}^{-1}]$ ),  $\phi$  is the potential (either  $[\text{m}]$  or  $[\text{V}]$ ),  
 318 and

$$319 \quad \mathbf{C} = \begin{bmatrix} C_{xx} & C_{xy} \\ C_{yx} & C_{yy} \end{bmatrix} \quad (9)$$

320

321 is the conductivity tensor (either  $[\text{m s}^{-1}]$  or  $[\text{S m}^{-1}]$ ).

322 Taking the component of the flux through the domain in a particular direction having unit  
 323 vector  $\hat{\mathbf{u}}_d$  and dividing by the magnitude of the potential gradient, we define

$$324 \quad C_d = -\frac{\mathbf{q} \cdot \hat{\mathbf{u}}_d}{|\nabla\phi|}, \quad (10)$$

325

326 where  $\cdot$  denotes the scalar product. Substitution of equation (8) into (10) yields

$$327 \quad C_d = -\frac{(-\mathbf{C} \nabla\phi) \cdot \hat{\mathbf{u}}_d}{|\nabla\phi|} = \hat{\mathbf{u}}_d^T \mathbf{C} \hat{\mathbf{u}}_g, \quad (11)$$

328

329 where  $\hat{\mathbf{u}}_g$  is a unit vector in the direction of the potential gradient. It is clear from equation (11)  
 330 that, using the boundary conditions illustrated in Figure 1c where the potential gradient is  
 331 along the  $x$  direction, measurement of  $C_d$  in the  $x$  and  $y$  directions will yield estimates  
 332 of conductivity tensor components  $C_{xx}$  and  $C_{yx}$ , respectively. Conversely, considering the  
 333 boundary conditions illustrated in Figure 1d where  $\hat{\mathbf{u}}_g$  is along the  $y$  direction, measurement  
 334 of  $C_d$  in the  $x$  and  $y$  directions will provide estimates of components  $C_{xy}$  and  $C_{yy}$ , respectively.

335 For each considered square domain size, we estimate  $C_{xx}$ ,  $C_{xy}$ ,  $C_{yx}$ , and  $C_{yy}$  for multiple  
 336 DFN realizations until stable estimates of the mean and variance of these tensor components  
 337 across the realizations are obtained. Figure 2 shows an example of the progression of the  
 338 mean and variance for the electrical conductivity as a function of the number of realizations  
 339 considered, for a domain size of  $12 \times 12$  m. The data presented in this figure correspond to  
 340 one of the test cases investigated in Section 3. As could be expected, we see that the curves  
 341 fluctuate quite significantly for low numbers of realizations, but then gradually approach fixed  
 342 values as the number of samples increases. For this particular example, 100 generated DFNs  
 343 appear to be sufficient to yield stable estimates of the mean and variance of the conductivity

344 tensor components. This number will tend to increase for smaller domain sizes, and decrease  
345 for larger domains, as it depends on how well the domain size represents the REV.

346 [Figure 2 about here.]

347 We next examine the stable mean and variance estimates as a function of domain size in  
348 order to assess how these values vary with changing scale, with the aim of identifying the  
349 equivalent conductivity tensor for the medium and ultimately the size of the REV. Figure 3  
350 shows an example of the values obtained for the electrical conductivity, again for one of the  
351 test cases investigated in Section 3, for domains having side lengths of  $L = 4, 8, 12,$  and  $16$  m.  
352 Note that the results shown in this figure are typical of our findings in each test case. Quite  
353 importantly, we see that with the exception of the smallest domain size ( $L = 4$  m), the mean  
354 values for the tensor components are consistent, suggesting that they will not change as the  
355 domain gets larger and are thus representative of the medium's large-scale effective behaviour.  
356 That is, although a single DFN realization may yield values of components  $C_{xx}, C_{xy}, C_{yx},$   
357 and  $C_{yy}$  that are far from the equivalent tensor values for the medium, and indeed which  
358 may not even correspond to an anisotropic conductivity tensor in the sense that  $C_{xy} \neq C_{yx},$   
359 the mean across multiple realizations will provide reasonable estimates of these components  
360 (Kanit et al., 2003). As a result, we use the mean tensor values for the largest domain size  
361 considered in our analysis ( $L = 16$  m) to determine the large-scale tensorial properties of  
362 the fracture network corresponding to a chosen statistical distribution of fracture positions,  
363 orientations, lengths, and apertures. The eigenvalues and eigenvectors of the equivalent tensor  
364 matrix are used to determine the maximum and minimum conductivity values and principal  
365 directions, respectively (Bear, 2013). With regard to the variability of the estimated tensor  
366 components, we see in Figure 3 that the standard deviations decrease as the domain size  
367 increases, which is expected because larger domains will better represent the overall medium  
368 properties. As discussed in the next section, the trend in conductivity variability with domain  
369 size allows us to establish a scaling relationship that is used to estimate the size of the REV.

370 [Figure 3 about here.]

## 371 2.5 Determination of the REV size

372 Cailletaud et al. (1994) and Kanit et al. (2003) proposed a combined statistical and numerical  
373 approach to the REV estimation problem, whereby a scaling relationship for the variance  
374 of the parameter of interest is established based on numerical simulations in order to define  
375 the size of the REV in terms of a prescribed level of statistical error. Originally used by  
376 the authors to investigate the bulk thermal and elastic properties of random composites, the  
377 approach has since been applied to a variety of other problems, including examination of the  
378 elastic and electrical behaviour of multi-scale high-contrast materials (Willot & Jeulin, 2011),  
379 quantification of the matrix clay content of rocks at the mesoscale (Keller, 2015), and the  
380 upscaling of seismic P- and S-wave moduli in fractured media (Caspari et al., 2016). A key  
381 tenet of the approach holds that the notion of a single REV size for a heterogeneous material  
382 should be abandoned. Instead, it is argued that the size of the REV must be considered  
383 within a statistical framework as its value will depend upon the level of error in the large-  
384 scale equivalent properties deemed acceptable, the physical property being considered and, in  
385 the case where the goal is estimation of the minimum domain size required to determine the  
386 macroscopic properties of the medium, the number of samples or realizations at that domain  
387 size that are available.

388 In our work, we wish to determine the minimum volume of fractured rock for which the  
389 electrical or hydraulic conductivity exhibited by that volume is representative of the equivalent  
390 tensor properties of the fractured domain, to within some level of error  $\epsilon$ . To simplify our  
391 analysis, we do not examine the variability of each conductivity tensor component individually,  
392 but rather that of the first invariant of the conductivity tensor given by  $I_C = C_{xx} + C_{yy}$   
393 (Li et al., 2009; Li & Zhang, 2010). The strong advantage of working with the invariant is  
394 that it is independent of the chosen coordinate system. Therefore the results obtained will  
395 not depend upon the orientation of the fracture network with respect to the applied boundary  
396 conditions. Assuming that  $I_C$  for a particular domain area  $S$  is a Gaussian distributed random  
397 variable with mean  $E\{I_C(S)\}$  and variance  $\text{Var}\{I_C(S)\}$ , a particular DFN realization at that  
398 domain size will have, with a 95% degree of confidence, an  $I_C$  value lying within a distance  $\epsilon$   
399 of the mean when  $\epsilon = 2\sqrt{\text{Var}\{I_C(S)\}}$ . In terms of the relative error  $\epsilon_r$ , this can be expressed

$$\epsilon_r = \frac{2\sqrt{\text{Var}\{I_C(S)\}}}{E\{I_C(S)\}}. \quad (12)$$

The REV for a chosen level of relative error  $\epsilon_r$  will be the domain size that has a variance satisfying equation (12). In order to find that domain size, we require knowledge of how  $\text{Var}\{I_C(S)\}$  changes as a function of  $S$ , which is obtained by fitting an assumed form of scaling relationship to the results of our numerical simulations on DFNs of various sizes.

Based on previous work (Cailletaud et al., 1994; Kanit et al., 2003; Lantuejoul, 1991), we postulate that the following power-law scaling relationship applies to the first invariant of the hydraulic and electrical conductivity tensors:

$$\text{Var}\{I_C(S)\} = \kappa S^{-\alpha}, \quad (13)$$

where  $\kappa$  and  $\alpha$  are fitting parameters that depend on the nature of the fracture network and physical property being studied. For properties such as the volumetric average or volume fraction, which represent an additive combination of the small-scale medium heterogeneities, classical geostatistical theory predicts that  $\alpha = 1$  and that  $\kappa$  will be equal to the product of the medium's integral range and the point-scale property variance (Chiles & Delfiner, 1999; Lantuejoul, 1991; Matheron, 1971). Properties like the electrical and hydraulic conductivity, however, are not additive meaning that, in general,  $\alpha \neq 1$ . Although the form of equation (13) cannot be proven for the electrical and hydraulic conductivities in fractured rock, a number of empirical studies have shown the suitability of this relationship for similar non-additive physical quantities (Cailletaud et al., 1994; Kanit et al., 2003; Lantuejoul, 1991; Willot & Jeulin, 2011). Furthermore, all of the test cases examined in Section 3 suggest that use of the power-law relationship is appropriate.

Substituting equation (13) into (12) and setting  $S = L^2$ , we estimate the size of the REV in terms of the square side length  $L$  as follows:

$$L = \left( \frac{2\sqrt{\kappa}}{\epsilon_r E\{I_C(S)\}} \right)^{1/\alpha}. \quad (14)$$



428 To determine parameters  $\kappa$  and  $\alpha$ , we (i) estimate the variance of  $I_C$  from the results of  
429 our numerical flow simulations on multiple DFN realizations for each studied domain size;  
430 (ii) make a log-log plot of  $\text{Var}\{I_C(S)\}$  versus  $S$ ; and (iii) determine the slope and intercept of  
431 the corresponding least-squares best-fitting line through the points. As an example, Figure 4  
432 shows a log-log plot of the variance of  $I_C$  versus domain area  $L^2$  for the electrical conductivity.  
433 Again, the results shown in this figure are typical of the different test cases considered in our  
434 study. We see that the points tend to fall along a straight line, whose slope and intercept  
435 allow us to estimate  $\alpha$  and  $\kappa$ , respectively.

436 [Figure 4 about here.]

### 437 **3 Results**

#### 438 **3.1 Test cases and analysis**

439 We now apply the analysis methodology presented in Section 2 to a total of 16 different test  
440 cases, where our goal is to examine how changes in the parameters governing the fracture  
441 distribution affect the REV size and equivalent tensor characteristics for the electrical and  
442 hydraulic conductivities. Table 1 summarizes each test case in terms of the angle, aperture,  
443 and length distributions considered for the two fracture sets. In Figure 5, we show example  
444 DFNs corresponding to each case for a  $16 \times 16$  m domain size, where the colour of the lines  
445 is used to quantify the fracture aperture. Finally, Figure 6a and 6b show histograms of the  
446 two truncated log-normal probability distributions for the aperture considered in Cases 12,  
447 13, and 14, whereas Figure 6c and 6d show histograms of the fracture length distributions for  
448 power-law exponent values of  $a = 2.0$  and  $a = 2.5$ , respectively.

449 [Table 1 about here.]

450 [Figure 5 about here.]

451 [Figure 6 about here.]

452 For the electrical conductivity, two scenarios are considered in our analysis. In the first  
453 scenario, which we believe to be most representative of real-world conditions, we assume a

454 rock matrix conductivity of  $\sigma_m = 10^{-4}$  S m<sup>-1</sup> and a fracture or groundwater conductivity  
 455 of  $\sigma_f = 10^{-1}$  S m<sup>-1</sup> (Schön, 2015). Here, the matrix plays an important and normal role in  
 456 the conduction of electric current through the rock as the ratio between the conductivities is  
 457  $\sigma_m/\sigma_f = 10^{-3}$  (Roubinet & Irving, 2014). In the second scenario, the matrix conductivity is  
 458 decreased to a value of  $\sigma_m = 10^{-7}$  S m<sup>-1</sup> such that the contribution of the matrix to electrical  
 459 conduction through the rock is negligible. The goal with this scenario, where  $\sigma_m/\sigma_f = 10^{-6}$ ,  
 460 is to have a test situation that allows us to assess the impact of the single power versus cubic  
 461 dependence on aperture of the fracture conductance and transmissivity, respectively, as well  
 462 as examine the role of the matrix on the REV size and equivalent tensor characteristics.

463 In our analysis, square domain sizes of  $L = 4, 8, 12,$  and  $16$  m were considered for each test  
 464 case to calibrate the scaling relationship for the tensor invariant in equation (14). A relative  
 465 error of  $\epsilon_r = 20\%$  was considered in our estimation of the REV size (Li et al., 2009; Li &  
 466 Zhang, 2010). The mean tensor components for the largest ( $16 \times 16$  m) domain size were used  
 467 to estimate the equivalent conductivity tensor. The number of realizations needed to obtain  
 468 stable mean and variance estimates of each tensor component was chosen as the point at which  
 469 the cumulative values did not vary more than 5 % over the last 20 samples (Figure 2). For  
 470 the fluid and electric current flow modeling, hydraulic head and electric potential differences  
 471 of 1 m and 1 V were applied across each considered DFN (Figure 1c and 1d). For the electric  
 472 current flow modeling, the rock matrix was discretized into square blocks of side length 2 m.

473 Table 2 shows the results obtained for each test case for the electrical conductivity ( $\sigma$ )  
 474 assuming  $\sigma_m/\sigma_f = 10^{-3}$ , whereas Table 3 shows the results obtained assuming  $\sigma_m/\sigma_f = 10^{-6}$ .  
 475 The corresponding results for the hydraulic conductivity ( $K$ ) are given in Table 4. In the tables  
 476 we provide (i) the estimated REV size; (ii) the maximum and minimum principal values of  
 477 the conductivity tensor; (iii) the corresponding conductivity anisotropy ratio; and (iv) the  
 478 direction of maximum conductivity. Note that the direction of maximum conductivity is only  
 479 given if the anisotropy is greater than 5%. Otherwise, the system is considered to be effectively  
 480 isotropic with no preferred orientation. Below we discuss how all of these quantities compare  
 481 between the electrical and hydraulic conductivities, as well as vary as we change details of the  
 482 statistical distributions for the fracture orientations, apertures, and lengths.

483 [Table 2 about here.]

484 [Table 3 about here.]

485 [Table 4 about here.]

### 486 **3.2 Effect of changing angle between the fracture sets**

487 We first consider Cases 1, 2, and 3 from Table 1, whereby the angle between the two fracture  
488 sets is changed by varying the mean orientation angle of Fracture Set 2. Figure 7 shows the  
489 impact of this change on the REV size (Figure 7a), the anisotropy ratio of the equivalent  
490 conductivity tensor (Figure 7b), the direction of maximum conductivity (Figure 7c), and the  
491 maximum conductivity value (Figure 7d). Note that the maximum conductivities plotted in  
492 Figure 7d were normalized by the values obtained for Case 1 in order to better compare the  
493 relative changes between the hydraulic and electrical conductivities.

494 [Figure 7 about here.]

495 We see in Figure 7a that, in accordance with previous work (Wang & Kulatilake, 2008),  
496 the size of the REV for the hydraulic conductivity decreases as the angle between the two  
497 fracture sets increases from 30 to 90 degrees. The curve for the electrical conductivity with  
498  $\sigma_m/\sigma_f = 10^{-6}$  is observed to exhibit exactly the same trend. This occurs because, as the  
499 range of fracture orientations in the medium increases, smaller domain sizes become able to  
500 support flow in all directions through the fracture network, thereby allowing those domain  
501 sizes to better represent the conductivity as an equivalent tensor. Indeed, in a fracture network  
502 where the angle between the two fracture sets is small, connectivity in all directions through  
503 the network will only be established for larger domain sizes because smaller domains will  
504 not allow sides of the network that are largely parallel to the fractures to be connected via  
505 the fractures. This implies a larger REV size. For the electrical conductivity scenario with  
506  $\sigma_m/\sigma_f = 10^{-3}$ , on the other hand, Figure 7a shows that the REV size is noticeably smaller and  
507 remains approximately constant as the angle between the fracture sets is increased. Quite  
508 importantly, the higher electrical conductivity of the matrix in this scenario has a strong  
509 homogenizing effect, meaning that the fractures are less critical for current flow through the

510 domain and the medium can thus be represented by an equivalent tensor at a 30-50% smaller  
511 scale. This strong reduction in the REV size for the  $\sigma_m/\sigma_f = 10^{-3}$  scenario, which we again  
512 believe to be more representative of realistic conditions than the  $\sigma_m/\sigma_f = 10^{-6}$  scenario in  
513 the sense that conduction through the rock matrix cannot be ignored, occurs in all of the  
514 16 test cases considered in our study (Tables 2 and 3). It has strong practical implications  
515 because it means that (i) the electrical conductivity can always be modeled as an equivalent  
516 tensor at a notably smaller scale than the hydraulic conductivity; and (ii) this tensor, for  
517 reasons of scale alone, is not likely to easily translate to the hydraulic conductivity.

518       Regarding the anisotropy of the equivalent conductivity tensor, we see in Figure 7b that,  
519 as expected, the degree of anisotropy tends to decrease as the angle between the two fracture  
520 sets increases from 30 to 90 degrees, with the case of two orthogonal fracture sets being  
521 effectively isotropic (Wang & Kulatilake, 2008). This decrease is seen to be greatest for  $K$   
522 and for the  $\sigma_m/\sigma_f = 10^{-6}$  scenario because the connectivity in these situations is controlled  
523 completely by the fractures. Because the apertures of Fracture Sets 1 and 2 are the same  
524 and there is an approximately equal number of fractures belonging to each set in the domain,  
525 the direction of maximum conductivity in all cases is seen to take the average of the mean  
526 orientations of these fracture sets (Figure 7c). The maximum conductivity in Figure 7d is  
527 observed to decrease slightly as the angles of Fracture Sets 1 and 2 diverge, with the changes  
528 being less pronounced when  $\sigma_m/\sigma_f = 10^{-3}$ .

### 529 **3.3 Effect of changing fracture angle variability**

530 We next examine Cases 2 and 4, where the variability of the orientation angle of both fracture  
531 sets is increased by changing the standard deviation from 5 to 10 degrees, respectively. The  
532 average angle between the fracture sets in both cases is 60 degrees (Table 1). Figure 8  
533 shows the corresponding results where we see that, despite that fact that the orientation  
534 angle variability is doubled between Cases 2 and 4, there are minor changes in the REV  
535 size, equivalent tensor anisotropy ratio, direction of maximum conductivity, and maximum  
536 conductivity value for both the hydraulic and electrical conductivities. Although this result  
537 is surprising given the findings of Long et al. (1982) and Wang & Kulatilake (2008), who saw

538 a reduction in the REV size and degree of anisotropy for the permeability with an increase  
539 in fracture orientation variability, it likely occurs because the range of angles covered by the  
540 fracture network in Case 2 is already quite extensive, and thus not significantly changed when  
541 the spread of the orientation angle of each fracture set is increased. Indeed, a comparison  
542 of the example DFNs for Cases 2 and 4 suggests that the differences in fracture-network  
543 connectivity are rather minimal (Figure 5). Again, we observe in Figure 8a that the REV  
544 size is 42-46% smaller for the  $\sigma_m/\sigma_f = 10^{-3}$  scenario. The degree of anisotropy is also less  
545 for this scenario (Figure 8b) because of the homogenizing effect of the matrix conductivity.

546 [Figure 8 about here.]

### 547 3.4 Effect of changing fracture aperture

548 In the next series of tests, we examine how changing the aperture of the fracture sets impacts  
549 the REV size and properties of the equivalent tensors for  $K$  and  $\sigma$ . We first consider Cases  
550 2 and 11, between which the aperture of Fracture Sets 1 and 2 is increased from 1 mm to  
551 1.5 mm (Table 1). Figure 9 shows the corresponding results. We see in Figure 9a that, for  
552 the hydraulic conductivity and for the electrical conductivity when  $\sigma_m/\sigma_f = 10^{-6}$ , a uniform  
553 increase in the fracture aperture has no impact on the REV size. This is because the domain  
554 properties are controlled completely by the fractures in these two situations, and uniformly  
555 increasing the flow through all of the fractures by changing their aperture should not affect  
556 the scale at which the fracture network can be effectively described by an anisotropic tensor.  
557 It will, however, increase the overall magnitude of the tensor components, which is clearly  
558 shown in Figure 9d with the largest relative change exhibited by  $K$  because of the cubic  
559 dependence of fracture hydraulic transmissivity on aperture (equation (5)). For the electrical  
560 conductivity when  $\sigma_m/\sigma_f = 10^{-3}$ , on the other hand, increasing the fracture aperture is seen  
561 to cause in a slight increase in the REV size. This occurs because the fractures account for a  
562 greater fraction of the total current flow through the rock when their aperture is larger, and  
563 thus the previously described homogenizing effect of the matrix conductivity, which again  
564 tends to decrease the REV size, is reduced. The lesser importance of matrix current flow  
565 with larger aperture also translates to a slight increase in the tensor anisotropy ratio for the

566  $\sigma_m/\sigma_f = 10^{-3}$  scenario (Figure 9b).

567 [Figure 9 about here.]

568 Next we consider Cases 2, 8, 9, and 10, where we investigate the effects of increasing  
569 the aperture of Fracture Set 2 while keeping the aperture of Fracture Set 1 fixed at 1 mm.  
570 The average angle between the fracture sets is 60 degrees (Table 1). Figure 10 shows the  
571 results obtained for the REV size and equivalent conductivity tensor as a function of the  
572 aperture of Fracture Set 2. We see in Figure 10a that, as the aperture increases, the size  
573 of the REV also increases because the second fracture set gradually begins to dominate the  
574 flow response, making the medium behave more like one having only a single set of fractures.  
575 The increase in REV size is greatest for  $K$  because of the cubic dependence of hydraulic  
576 transmissivity on aperture, whereas for  $\sigma_m/\sigma_f = 10^{-6}$  only a small change is observed. For  
577 the electrical conductivity scenario where  $\sigma_m/\sigma_f = 10^{-3}$ , the increase in REV size is slightly  
578 greater because the fractures carry a larger fraction of the total current flow compared to the  
579 matrix as the aperture of Fracture Set 2 is increased.

580 [Figure 10 about here.]

581 With regard to the equivalent conductivity tensor characteristics, the change in aperture  
582 of Fracture Set 2 is seen to have significant effects on the anisotropy ratio (Figure 10b),  
583 the direction of maximum conductivity (Figure 10c), and the maximum conductivity value  
584 (Figure 10d), with the changes for  $K$  being greater than those for  $\sigma$ , again because of the  
585 much stronger dependence of fluid flow upon aperture through the cubic law. In Figure 10b,  
586 we see that the anisotropy ratio for  $K$  first decreases as the aperture of Fracture Set 2 is  
587 increased from 1 mm to 1.1 mm, but then increases sharply as the aperture approaches 2 mm.  
588 This can be explained by the fact that, when the apertures of Fracture Sets 1 and 2 are equal  
589 (Case 2) there is already substantial anisotropy along a 30-degree orientation exhibited by  
590 the equivalent  $K$  tensor. As the aperture of Fracture Set 2, which has a mean orientation  
591 of 60 degrees, is increased (Case 8), the initial tendency is to reduce the existing anisotropy  
592 by stretching the tensor ellipse away from the direction of maximum conductivity. When the  
593 aperture is increased further, however, Fracture Set 2 eventually dominates the flow response

594 (Case 10), causing strong anisotropy along a different, 60-degree orientation. With regard to  
595  $\sigma$ , the same general trend with increasing aperture is observed except that, because of the  
596 weaker dependence of electric current flow upon aperture compared to fluid flow, a 2 mm  
597 aperture for Fracture Set 2 (Case 10) is not yet large enough for this fracture set to dominate  
598 the flow response and cause anisotropy along the 60-degree orientation. As a result, we see  
599 only the system becoming more isotropic as the aperture of Fracture Set 2 is increased.

600 In Figure 10c, we observe one of the most important results of our analysis, which is that  
601 the maximum principal direction of the equivalent tensor can be significantly different between  
602 the hydraulic and electrical conductivities when the aperture distribution between the fracture  
603 sets is not the same. When both fracture sets share the same 1-mm constant aperture, for  
604 example, the directions of maximum conductivity for  $K$  and  $\sigma$  are seen to be identical and  
605 equal to 30 degrees, the average value between the mean orientations of the two fracture sets.  
606 As the aperture of Fracture Set 2 is increased, however, the principal orientations between  
607  $K$  and  $\sigma$  diverge because fluid flow through the domain is affected much more than electric  
608 current flow, meaning that the maximum principal direction of the  $K$  tensor moves more  
609 quickly towards the 60-degree orientation. This finding, which is admittedly rather intuitive,  
610 has significant implications for studies where researchers have attempted to infer principal  
611 groundwater flow directions from the results of azimuthal resistivity surveys in fractured rock  
612 (Ritzi & Andolsek, 1992; Skinner & Heinson, 2004; Skjerna & Jørgensen, 1994; Steinich &  
613 Marin, 1996; Yeboah-Forson & Whitman, 2014). Specifically, our results indicate that only  
614 in very specific circumstances can the principal directions of the electrical conductivity tensor  
615 be expected to provide meaningful information regarding those of the hydraulic conductivity  
616 tensor. Further, the ratio and trends observed in the maximum and minimum principal  
617 conductivity values will, in general, vary significantly between  $K$  and  $\sigma$  (Figure 10b and 10d).

618 Finally, we consider Cases 3, 5, 6, and 7, where we again increase only the aperture of  
619 Fracture Set 2, but this time considering an average angle between the fracture sets of 90  
620 degrees. Figure 11 shows the corresponding results for the REV size and equivalent conduc-  
621 tivity tensor characteristics. As we observed in Figure 10, the REV size for  $K$  is seen to  
622 increase with an increase in the aperture of Fracture Set 2 because this fracture set quickly

623 begins to dominate the flow response as a result of the cubic law. The changes in REV size  
 624 for the  $\sigma_m/\sigma_f = 10^{-3}$  and  $\sigma_m/\sigma_f = 10^{-6}$  scenarios, on the other hand, are again rather  
 625 negligible (Figure 11a). As there is no anisotropy when the apertures of the two fracture  
 626 sets are equal (Case 3), the anisotropy ratio is seen to consistently increase as the aperture of  
 627 Fracture Set 2 increases (Figure 11b), with the direction of maximum conductivity in all cases  
 628 being approximately equal to 90 degrees, which is the mean orientation of the second fracture  
 629 set (Figure 11c). In other words, making the aperture of Fracture Set 2 larger in this case  
 630 immediately results in anisotropy along the 90-degree orientation, with the greatest increase  
 631 in anisotropy being exhibited by  $K$ . Similarly, the maximum conductivity value is seen to  
 632 increase most for  $K$  with an increase in the aperture of the second fracture set (Figure 11d),  
 633 which again results from the greater sensitivity of fluid flow to fracture aperture as compared  
 634 to electric current flow.

635 [Figure 11 about here.]

### 636 3.5 Effect of changing fracture aperture variability

637 We now investigate how changing the variability of the aperture distribution of both fracture  
 638 sets affects the REV size and equivalent tensor characteristics for the electrical and hydraulic  
 639 conductivities. To this end, we examine Cases 2, 12, and 13, which involve a constant aper-  
 640 ture and two truncated log-normal aperture distributions having different spreads (Table 1).  
 641 The histograms for the log-normal distributions considered in Cases 12 and 13 are shown  
 642 in Figure 6a and 6b, respectively, where we see that the choice of parameters for the mean  
 643 and variance of the natural logarithm of the aperture are such that the peak value remains  
 644 constant and equal to 1 mm, but the dispersion around this value changes. Figure 12 shows  
 645 the corresponding results. In Figure 12a we observe that, as the spread of the aperture dis-  
 646 tribution of both fracture sets increases, the REV size for  $K$  increases, whereas the REV  
 647 sizes for the  $\sigma_m/\sigma_f = 10^{-3}$  and  $\sigma_m/\sigma_f = 10^{-6}$  scenarios exhibit minimal changes. Again,  
 648 because of the strong dependence of hydraulic transmissivity on fracture aperture compared  
 649 to the electrical conductance, the fluid flow behaviour of the network will be greatly influ-  
 650 enced by randomly distributed, large-aperture fractures, which become more prevalent when



651 the fracture aperture spread is increased (Figure 5). To account for this increased variability,  
652 the domain size required to represent the flow response using an equivalent  $K$  tensor must  
653 increase (Baghbanan & Jing, 2007; Long et al., 1982). Note, however, that no meaningful  
654 changes in the anisotropy ratio and principal directions of the  $K$  and  $\sigma$  tensors are observed  
655 as the spread of the aperture distribution increases (Figure 12b and 12c). This is because the  
656 same aperture distribution was considered for the two fracture sets in Cases 2, 12, and 13,  
657 and there is no reason to expect that changes in this distribution would lead to changes in  
658 the medium anisotropic characteristics. Conversely, we see in Figure 12d that an increased  
659 variability in fracture aperture results in an increase in the overall conductivity magnitude,  
660 as the presence of a greater number of large-aperture fractures will increase the amount of  
661 fluid and electric current flow through the domain. This is most significant for  $K$  because of  
662 the cubic law.

663 [Figure 12 about here.]

### 664 **3.6 Effect of correlation between aperture and length**

665 Our second-last test involves examination of the impact of correlation between fracture aper-  
666 ture and length on the REV size and equivalent tensor properties. As mentioned previously,  
667 there is significant empirical and theoretical evidence to support fracture apertures being  
668 positively correlated with their length. This prompted an investigation into the effects of  
669 correlation between these two variables on the REV size and tensor characteristics for the  
670 permeability (Baghbanan & Jing, 2007), but never before for the electrical conductivity. In  
671 this regard, we now consider Cases 12 and 14, which involve the same truncated log-normal  
672 distribution for the fracture aperture in the absence and presence of correlation between  
673 aperture and length, respectively. Figure 13 shows the results obtained, where correlation is  
674 indicated on the horizontal axis using a binary variable (0 = uncorrelated; 1 = correlated).  
675 We see in the figure that, as expected, correlation between aperture and length has no impact  
676 on the anisotropic characteristics of the equivalent  $K$  and  $\sigma$  tensors (Figure 13b and 13c).  
677 However, in accordance with Baghbanan & Jing (2007), it does lead to an increase in the REV  
678 size (Figure 13a) as well as the overall conductivity magnitudes (Figure 13d). The latter find-

ings are explained by the fact that correlation between aperture and length means that longer fractures in the domain will be associated with larger apertures (Figure 5), which greatly increases the probability that the fluid and electric current flow behaviour will be dominated by a small number of long fractures, as opposed to being more equally influenced by all of the fractures in the network. As a result, the size of the REV must increase to accommodate the increased variability in the flow response, with the change in REV size being greatest for  $K$  and for  $\sigma_m/\sigma_f = 10^{-6}$  where flow through the matrix is negligible. The overall conductivity magnitudes must also increase because flow through the domain will be facilitated by the long, large-aperture fractures, especially for  $K$ .

[Figure 13 about here.]

### 3.7 Effect of changing fracture length power-law exponent

Finally, we examine the impact of the fracture length power-law exponent  $a$  from equation (1). To this end, we consider Cases 2, 15, and 16, where  $a$  is increased from 2.0 to 2.5 while keeping the other fracture-network parameters constant (Table 1). Figure 6c and 6d show histograms of the fracture length distribution for values of  $a = 2.0$  and  $a = 2.5$ , respectively, where we see that increasing the power-law exponent results in a greater proportion of shorter fractures throughout the domain (see also Figure 5). The impact of this change on the REV size and equivalent  $K$  and  $\sigma$  tensor characteristics is shown in Figure 14. We observe in Figure 14a that, as the value of  $a$  increases and connectivity across the domain becomes dependent upon a smaller number of randomly distributed long fractures, the REV sizes for  $K$  and for the  $\sigma_m/\sigma_f = 10^{-6}$  scenario increase by a factor of approximately 5. As flow occurs purely through the fracture network, a larger domain size is required to accommodate the greater variability in flow behaviour and represent the network as an equivalent tensor quantity. Conversely, for the electrical conductivity when  $\sigma_m/\sigma_f = 10^{-3}$ , there is only a slight increase in the REV size with increasing  $a$  value (Table 2) because the electric current flow through the matrix permits connections across the domain independently of the fracture network, thereby reducing the importance of the latter. With regard to the tensor anisotropy ratio, Figure 14b shows a gradual decrease with increasing power-law exponent, which likely results because the smaller

707 number of long fractures tends to reduce the directionality of the flow response. As expected,  
708 the direction of maximum conductivity is not affected by the change in power-law exponent  
709 (Figure 6c) and is equal, as before, to the average value of the mean orientations of the two  
710 fracture sets. Finally, in Figure 14d we see that increasing the fracture length power-law  
711 exponent has the effect of reducing the maximum principal conductivity value for both  $K$   
712 and  $\sigma$ , as connectivity across the domain is notably reduced. Because of the contribution of  
713 the matrix, this reduction is less pronounced for the  $\sigma_m/\sigma_f = 10^{-3}$  scenario.

714 [Figure 14 about here.]

## 715 4 Discussion and conclusions

716 We have presented in this paper a systematic analysis of the effects of changes in the statistical  
717 parameters governing fracture networks on the REV size and equivalent tensor characteristics  
718 for the electrical and hydraulic conductivities. Thanks to the recently developed DDP mod-  
719 eling approach of Roubinet & Irving (2014), electric current flow through arbitrarily complex  
720 fractured domains can be simulated efficiently and accurately, properly taking into account  
721 important contributions to current flow through the matrix as well as between the fractures  
722 and matrix. Groundwater flow, on the other hand, was simulated in our work using a stan-  
723 dard DFN methodology based on the usual assumption that matrix fluid flow is negligible due  
724 to the many-orders-of-magnitude difference between the hydraulic properties of the matrix  
725 and those of the fractures. One strong advantage of the combined statistical and numerical  
726 analysis approach considered in this paper, which builds on the seminal work of Cailletaud  
727 et al. (1994) and Kanit et al. (2003), is that numerical flow simulations need not be performed  
728 at the REV scale in order to estimate the REV size and equivalent tensor properties. That  
729 is, we can conduct the entire REV analysis using smaller, less computationally burdensome,  
730 domain sizes whose statistical characteristics can then be linked to those of the REV. The  
731 approach also has the advantage of explicitly treating the REV size as a stochastic quantity,  
732 whose estimated value depends upon the error in large-scale equivalent properties that one  
733 is willing to accept. Although these advantages do come at the cost of needing to define in

734 advance a scaling relationship for the conductivity variability, all of the results obtained in  
735 this paper suggest that our assumption of power-law scaling is appropriate.

736 Two key differences between groundwater and electric current flow in fractured rock were  
737 seen to lead to significant differences in the REV size and tensor characteristics between the  
738 electrical and hydraulic conductivities. First, matrix flow must be considered in the electrical  
739 case, which tends to have a homogenizing effect on the flow response in the sense that, because  
740 the matrix is responsible for a significant fraction of the total current passing through the  
741 rock, the effect of the fractures will be less pronounced. Secondly, whereas the hydraulic  
742 transmissivity of a fracture varies with the cube of its aperture, the analogous electrical  
743 conductance varies only linearly with the aperture. As a result of these two differences we  
744 observed that: (i) the REV size and degree of anisotropy are consistently less for the electrical  
745 conductivity than for the hydraulic conductivity for realistic matrix-to-fracture conductivity  
746 ratios (e.g., the considered  $\sigma_m/\sigma_f = 10^{-3}$  scenario); (ii) changes in the angle, aperture,  
747 and length distributions of the fracture network have a stronger effect on  $K$  than on  $\sigma$ , in  
748 particular with regard to the aperture; and (iii) in the presence of more than one fracture  
749 set, the principal directions of the equivalent electrical conductivity tensor do not generally  
750 correspond with those of the equivalent hydraulic conductivity tensor, and in fact can vary by a  
751 significant amount. Consequently, attempting to make conclusions about the hydrogeological  
752 properties of fractured domains based on geoelectrical measurements, as has been attempted in  
753 many previous studies, must be done with great caution. It cannot, for example, be generally  
754 assumed that the degree and direction of electrical conductivity anisotropy, estimated from an  
755 azimuthal resistivity survey, will provide useful information on hydraulic anisotropy. Further,  
756 changes observed in  $\sigma$  across a domain cannot be interpreted in terms of changes in  $K$ , except  
757 in a highly qualitative manner. Finally, variations in fracture aperture that have a strong  
758 effect on fluid flow may have minimal influence on geoelectrical measurements, meaning that  
759 ER data will be of limited use to assess many important hydraulic characteristics. Note  
760 that, although our results were obtained for the DC resistivity, we expect them to be equally  
761 applicable to EM-based investigations, where directional properties of the conductivity at low  
762 frequencies have been interpreted hydrogeologically (Steelman et al., 2015).

763 It is important to emphasize that, for all of the analyses carried out in this paper, we  
764 considered boundary conditions corresponding to a linear potential gradient across the frac-  
765 tured domain, which are fully consistent with previous hydrogeological research aimed at  
766 assessing the intrinsic equivalent properties of the fracture network along with the REV size  
767 (Baghbanan & Jing, 2007; Long et al., 1982; Min et al., 2004; Wang & Kulatilake, 2008).  
768 Although such linear potential gradients are likely to exist away from point sources such as  
769 pumping or injection wells and current electrodes, boundary conditions in the vicinity of these  
770 sources will differ and therefore also the flow of water or electric current through the fracture  
771 network. As a result, an important topic of future research is the investigation of how the  
772 key differences between the hydraulic and electrical conductivities highlighted in this work are  
773 manifested in real-world field experiments to measure these properties, which typically involve  
774 pumping/injection experiments and the use of point electrodes, respectively. To this end, we  
775 are currently developing numerical modeling codes for the accurate simulation of azimuthal  
776 resistivity measurements in 3D fractured-rock environments.

777 We also note that the numerical values for the REV size determined in this paper are  
778 not nearly as important as the trends in REV size observed as a function of changes in  
779 fracture-network properties, as well as how results compare between the hydraulic and elec-  
780 trical conductivities. Indeed, the estimated REV size depends on many factors, most notable  
781 of which are the fracture density and prescribed level of error in equivalent properties con-  
782 sidered to be acceptable. Further, we have not addressed in this paper the question of the  
783 existence of the REV, which may not occur for some fracture networks or may happen at a  
784 variety of different scales (Long et al., 1982). It should also be pointed out that, as much as  
785 we have considered the effects of changing a variety of fracture properties (i.e., orientation,  
786 aperture, length) as well as the matrix-to-fracture electrical conductivity ratio in this paper,  
787 it is the overall difference between the effective fracture network conductance, which depends  
788 on all of these factors, and the matrix conductance that will tend to control the homogenizing  
789 effects observed. Finally, as in other related DFN studies for the permeability, we have not  
790 examined in this paper the effects of aperture variability within a fracture and the impact  
791 of fracture filling or alteration. Initial investigations into these issues could be performed

792 with the considered DDP and DFN numerical modeling approaches by dividing individual  
793 fractures into sub-fractures having different properties. This is a topic of future work.

## 794 **Acknowledgements**

795 This work was funded by a grant to J. Irving from the Swiss National Science Foundation  
796 (Number 200021\_143758).

## 797 References

- 798 Al Hagrey, S. A., 1994. Electric study of fracture anisotropy at Falkenberg, Germany, *Geo-*  
799 *physics*, **59**(6), 881–888.
- 800 Baghbanan, A. & Jing, L., 2007. Hydraulic properties of fractured rock masses with corre-  
801 lated fracture length and aperture, *International Journal of Rock Mechanics and Mining*  
802 *Sciences*, **44**(5), 704–719.
- 803 Bear, J., 2013. *Dynamics of fluids in porous media*, Courier Corporation.
- 804 Berkowitz, B., 2002. Characterizing flow and transport in fractured geological media: A  
805 review, *Advances in Water Resources*, **25**(8–12), 861–884.
- 806 Berryman, J. G. & Hoversten, G. M., 2013. Modelling electrical conductivity for earth media  
807 with macroscopic fluid-filled fractures, *Geophysical Prospecting*, **61**(2), 471–493.
- 808 Beskardes, G. D. & Weiss, C. J., 2018. Modelling DC responses of 3D complex fracture  
809 networks, *Geophysical Journal International*.
- 810 Boadu, F., Gyamfi, J., & Owusu, E., 2005. Determining subsurface fracture characteristics  
811 from azimuthal resistivity surveys: A case study at Nsawam, Ghana, *Geophysics*, **70**(5),  
812 B35–B42.
- 813 Boadu, F. K., Owusu-Nimo, F., & Menyeh, A., 2008. Nitrate contamination in groundwater  
814 at farmlands in Nsawam, Ghana: the role of fractures from azimuthal resistivity surveys,  
815 *Journal of Environmental & Engineering Geophysics*, **13**(1), 27–37.
- 816 Bonnet, E., Bour, O., Odling, N. E., Davy, P., Main, I., Cowie, P., & Berkowitz, B., 2001.  
817 Scaling of fracture systems in geological media, *Reviews of Geophysics*, **39**(3), 347–383.
- 818 Bour, O. & Davy, P., 1997. Connectivity of random fault networks following a power law fault  
819 length distribution, *Water Resources Research*, **33**(7), 1567–1583.
- 820 Brown, S. R., 1989. Transport of fluid and electric current through a single fracture, *Journal*  
821 *of Geophysical Research: Solid Earth*, **94**(B7), 9429–9438.
- 822 Busby, J., 2000. The effectiveness of azimuthal apparent-resistivity measurements as a method  
823 for determining fracture strike orientations, *Geophysical Prospecting*, **48**(4), 677–695.
- 824 Caballero Sanz, V., Roubinet, D., Demirel, S., & Irving, J., 2017. 2.5-D discrete-dual-porosity  
825 model for simulating geoelectrical experiments in fractured rock, *Geophysical Journal In-*  
826 *ternational*, **209**(2), 1099–1110.
- 827 Cacas, M., Ledoux, E., de Marsily, G., Tillie, B., Barbreau, A., Durand, E., Feuga, B.,  
828 & Peaudecerf, P., 1990. Modeling fracture flow with a stochastic discrete fracture net-  
829 work: Calibration and validation: 1. The flow model, *Water Resources Research*, **26**(3),  
830 doi:10.1029/WR026i003p00479.
- 831 Cailletaud, G., Jeulin, D., & Rolland, P., 1994. Size effect on elastic properties of random  
832 composites, *Engineering Computations*, **11**(2), 99–110.

- 833 Carneiro, J. F., 2009. Numerical simulations on the influence of matrix diffusion to carbon  
834 sequestration in double porosity fissured aquifers, *International Journal of Greenhouse Gas*  
835 *Control*, **3**(4), 431–443.
- 836 Caspari, E., Milani, M., Rubino, J., Müller, T. M., Quintal, B., & Holliger, K., 2016. Nu-  
837 merical upscaling of frequency-dependent P- and S-wave moduli in fractured porous media,  
838 *Geophysical Prospecting*, **64**(4), 1166–1179.
- 839 Chiles, J. P. & Delfiner, P., 1999. *Geostatistics: Modeling Spatial Uncertainty*, John Wiley &  
840 Sons, New York.
- 841 Cvetkovic, V., 2017. Statistical formulation of generalized tracer retention in fractured rock,  
842 *Water Resources Research*, **53**(11), 8736–8759.
- 843 Davy, P., Le Goc, R., Darcel, C., Bour, O., De Dreuzy, J.-R., & Munier, R., 2010. A likely  
844 universal model of fracture scaling and its consequence for crustal hydromechanics, *Journal*  
845 *of Geophysical Research: Solid Earth*, **115**(B10).
- 846 de Dreuzy, J.-R., Davy, P., & Bour, O., 2001. Hydraulic properties of two-dimensional random  
847 fracture networks following a power law length distribution: 1. Effective connectivity, *Water*  
848 *Resources Research*, **37**(8), 2065–2078.
- 849 DesRoches, A. J., Butler, K. E., & MacQuarrie, K. T., 2017. Surface self-potential patterns  
850 related to transmissive fracture trends during a water injection test, *Geophysical Journal*  
851 *International*, **212**(3), 2047–2060.
- 852 Devroye, L., 1986. *Non-Uniform Random Variate Generation*, Springer-Verlag.
- 853 Dey, A. & Morrison, H., 1979. Resistivity modeling for arbitrarily shaped two-dimensional  
854 structures, *Geophysical Prospecting*, **27**(1), 106–136.
- 855 Donadille, J.-M. & Al-Ofi, S., 2012. Crosswell electromagnetic response in a fractured medium,  
856 *Geophysics*, **77**(3), D53–D61, doi:10.1190/geo2011-0227.1.
- 857 Dorn, C., Linde, N., Doetsch, J., Borgne, T. L., & Bour, O., 2012. Fracture imaging within  
858 a granitic rock aquifer using multiple-offset single-hole and cross-hole GPR reflection data,  
859 *Journal of Applied Geophysics*, **78**, 123–132, doi:10.1016/j.jappgeo.2011.01.010.
- 860 Everett, M. E., 2013. *Near-Surface Applied Geophysics*, Cambridge University Press.
- 861 Follin, S., Hartley, L., Rhén, I., Jackson, P., Joyce, S., Roberts, D., & Swift, B., 2014. A  
862 methodology to constrain the parameters of a hydrogeological discrete fracture network  
863 model for sparsely fractured crystalline rock, exemplified by data from the proposed high-  
864 level nuclear waste repository site at Forsmark, Sweden, *Hydrogeology Journal*, **22**(2), 313–  
865 331.
- 866 Geiger, S. & Emmanuel, S., 2010. Non-Fourier thermal transport in fractured geological  
867 media, *Water Resources Research*, **46**(7), W07504.
- 868 Gisladdottir, V. R., Roubinet, D., & Tartakovsky, D. M., 2016. Particle methods for heat  
869 transfer in fractured media, *Transport in Porous Media*, **115**(2), 311–326.



- 870 Greenhalgh, S., Zhou, B., Greenhalgh, M., Marescot, L., & Wiese, T., 2009. Explicit expres-  
871 sions for the Fréchet derivatives in 3D anisotropic resistivity inversion, *Geophysics*, **74**(3),  
872 F31–F43.
- 873 Hatton, C., Main, I., & Meredith, P., 1994. Non-universal scaling of fracture length and  
874 opening displacement, *Nature*, **367**(6459), 160.
- 875 Herwanger, J., Worthington, M., Lubbe, R., Binley, A., & Khazanehdari, J., 2004a. A com-  
876 parison of cross-hole electrical and seismic data in fractured rock, *Geophysical Prospecting*,  
877 **52**(2), 109–121.
- 878 Herwanger, J. V., Pain, C. C., Binley, A., De Oliveira, C. R. E., & Worthington, M. H., 2004b.  
879 Anisotropic resistivity tomography, *Geophysical Journal International*, **158**(2), 409–425.
- 880 Jinsong, S., Benyu, S., & Naichuan, G., 2009. Anisotropic characteristics of electrical responses  
881 of fractured reservoir with multiple sets of fractures, *Petroleum Science*, **6**(2), 127–138.
- 882 Kanit, T., Forest, S., Galliet, I., Mounoury, V., & Jeulin, D., 2003. Determination of the  
883 size of the representative volume element for random composites: statistical and numerical  
884 approach, *International Journal of Solids and Structures*, **40**(13-14), 3647–3679.
- 885 Keller, L. M., 2015. On the representative elementary volumes of clay rocks at the mesoscale,  
886 *Journal of Geology and Mining Research*, **7**(6), 58–64.
- 887 Klimczak, C., Schultz, R. A., Parashar, R., & Reeves, D. M., 2010. Cubic law with aperture-  
888 length correlation: Implications for network scale fluid flow, *Hydrogeology Journal*, **18**(4),  
889 851–862.
- 890 Kolditz, O. & Clauser, C., 1998. Numerical simulation of flow and heat transfer in fractured  
891 crystalline rocks: Application to the Hot Dry Rock site in Rosemanowes (UK), *Geothermics*,  
892 **27**(1), 1–23.
- 893 Lane, J., Haeni, F., & Watson, W., 1995. Use of a square-array direct-current resistivity  
894 method to detect fractures in crystalline bedrock in New Hampshire, *Ground Water*, **33**(3),  
895 476–485.
- 896 Lantuejoul, C., 1991. Ergodicity and integral range, *Journal of Microscopy*, **161**(3), 387–403.
- 897 Lapcevic, P., Novakowski, K. S., & Sudicky, E., 1997. *Groundwater flow and solute transport*  
898 *in fractured media*, National Water Research Institute.
- 899 Li, J. & Zhang, L., 2010. Geometric parameters and REV of a crack network in soil, *Computers*  
900 *and Geotechnics*, **37**(4), 466–475.
- 901 Li, J., Zhang, L., Wang, Y., & Fredlund, D., 2009. Permeability tensor and representative  
902 elementary volume of saturated cracked soil, *Canadian Geotechnical Journal*, **46**(8), 928–  
903 942.
- 904 Li, Y. & Spitzer, K., 2005. Finite element resistivity modelling for three-dimensional structures  
905 with arbitrary anisotropy, *Physics of the Earth and Planetary Interiors*, **150**(1), 15–27.

- 906 Long, J. C. S., Remer, J. S., Wilson, C. R., & Witherspoon, P. A., 1982. Porous media  
907 equivalents for networks of discontinuous fractures, *Water Resources Research*, **18**(3), 645–  
908 658.
- 909 Maillot, J., Davy, P., Le Goc, R., Darcel, C., & de Dreuzy, J., 2016. Connectivity, permeability,  
910 and channeling in randomly distributed and kinematically defined discrete fracture network  
911 models, *Water Resources Research*, **52**(11), 8526–8545.
- 912 Manna, F., Walton, K. M., Cherry, J. A., & Parker, B. L., 2017. Mechanisms of recharge in  
913 a fractured porous rock aquifer in a semi-arid region, *Journal of Hydrology*, **555**, 869–880.
- 914 Marescot, L., Monnet, R., & Chapellier, D., 2008. Resistivity and induced polarization surveys  
915 for slope instability studies in the Swiss Alps, *Engineering Geology*, **98**(1-2), 18–28.
- 916 Matheron, G., 1971. *The Theory of Regionalized Variables and Its Applications*, Cen-  
917 tre de Morphologie Mathématique Fontainebleau: Les cahiers du Centre de Morphologie  
918 Mathématique de Fontainebleau, École National Supérieure des Mines.
- 919 Min, K.-B., Jing, L., & Stephansson, O., 2004. Determining the equivalent permeability  
920 tensor for fractured rock masses using a stochastic REV approach: Method and application  
921 to the field data from Sellafield, UK, *Hydrogeology Journal*, **12**(5), 497–510.
- 922 NAP, 2015. *Characterization, Modeling, Monitoring, and Remediation of Fractured Rock*,  
923 National Academies of Sciences, Engineering, and Medicine. National Academies Press,  
924 Washington, DC.
- 925 Neuman, S., 2005. Trends, prospects and challenges in quantifying flow and transport through  
926 fractured rocks, *Hydrogeology Journal*, **13**(1), 124–147.
- 927 Neuman, S. P., 2008. Multiscale relationships between fracture length, aperture, density and  
928 permeability, *Geophysical Research Letters*, **35**(22).
- 929 Olson, J. E., 2003. Sublinear scaling of fracture aperture versus length: An exception or the  
930 rule?, *Journal of Geophysical Research: Solid Earth*, **108**(B9).
- 931 Pain, C. C., Herwanger, J. V., Saunders, J. H., Worthington, M. H., & de Oliveira, C. R.,  
932 2003. Anisotropic resistivity inversion, *Inverse Problems*, **19**(5), 1081.
- 933 Pidlisecky, A. & Knight, R., 2008. FW2.5D: A MATLAB 2.5-D electrical resistivity modeling  
934 code, *Computers & Geosciences*, **34**(12), 1645–1654.
- 935 Porsani, J. L., Elis, V. R., & Hiodo, F. Y., 2005. Geophysical investigations for the character-  
936 ization of fractured rock aquifers in Itu, SE Brazil, *Journal of Applied Geophysics*, **57**(2),  
937 119–128.
- 938 Pytharouli, S., Lunn, R., Shipton, Z., Kirkpatrick, J., & do Nascimento, A., 2011. Microseis-  
939 micity illuminates open fractures in the shallow crust, *Geophysical Research Letters*, **38**(2),  
940 doi:10.1029/2010GL045875.
- 941 Renshaw, C. & Park, J., 1997. Effect of mechanical interactions on the scaling of fracture  
942 length and aperture, *Nature*, **386**(6624), 482.

- 943 Ritz, R. W. & Andolsek, R. H., 1992. Relation between anisotropic transmissivity and  
944 azimuthal resistivity surveys in shallow, fractured, carbonate flow systems, *Ground Water*,  
945 **30**(5), 774–780.
- 946 Robert, T., Dassargues, A., Brouyère, S., Kaufmann, O., Hallet, V., & Nguyen, F., 2011.  
947 Assessing the contribution of electrical resistivity tomography (ERT) and self-potential  
948 (SP) methods for a water well drilling program in fractured/karstified limestones, *Journal*  
949 *of Applied Geophysics*, **75**(1), 42–53.
- 950 Robert, T., Caterina, D., Deceuster, J., Kaufmann, O., & Nguyen, F., 2012. A salt tracer  
951 test monitored with surface ERT to detect preferential flow and transport paths in frac-  
952 tured/karstified limestones, *Geophysics*, **77**(2), B55–B67.
- 953 Rotter, B. E., Barry, D. A., Gerhard, J. I., & Small, J. S., 2008. Modeling U(VI) biomineral-  
954 ization in single- and dual-porosity porous media, *Water Resources Research*, **44**(8).
- 955 Roubinet, D. & Irving, J., 2014. Discrete-dual-porosity model for electric current flow in  
956 fractured rock, *Journal of Geophysical Research: Solid Earth*, **119**(2), 767–786.
- 957 Roubinet, D., Linde, N., Jougnot, D., & Irving, J., 2016. Streaming potential modeling in  
958 fractured rock: Insights into the identification of hydraulically active fractures, *Geophysical*  
959 *Research Letters*, **43**(10), 4937–4944.
- 960 Rücker, C., Günther, T., & Spitzer, K., 2006. Three-dimensional modelling and inversion of  
961 DC resistivity data incorporating topography - I. Modelling, *Geophysical Journal Interna-*  
962 *tional*, **166**, 495–505.
- 963 Schmutz, M., Ghorbani, A., Vaudelet, P., & Revil, A., 2011. Spectral induced polarization  
964 detects cracks and distinguishes between open- and clay-filled fractures, *Journal of Envi-*  
965 *ronmental and Engineering Geophysics*, **16**(2), 85–91, doi:10.1190/geo2011-0227.1.
- 966 Schön, J. H., 2015. *Physical Properties of Rocks: Fundamentals and Principles of Petro-*  
967 *physics*, vol. 65, Elsevier.
- 968 Sharma, S. & Baranwal, V., 2005. Delineation of groundwater-bearing fracture zones in a  
969 hard rock area integrating very low frequency electromagnetic and resistivity data, *Journal*  
970 *of Applied Geophysics*, **57**(2), 155–166.
- 971 Singhal, B. B. S. & Gupta, R. P., 2010. *Applied hydrogeology of fractured rocks*, Springer  
972 Science & Business Media.
- 973 Skinner, D. & Heinson, G., 2004. A comparison of electrical and electromagnetic methods  
974 for the detection of hydraulic pathways in a fractured rock aquifer, Clare Valley, South  
975 Australia, *Hydrogeology Journal*, **12**(5), 576–590.
- 976 Skjærnaa, L. & Jørgensen, N. O., 1994. Evaluation of local fracture systems by azimuthal  
977 resistivity surveys: Examples from South Norway, *Applied Hydrogeology*, **2**(2), 19–25.
- 978 Snow, D. T., 1969. Anisotropic permeability of fractured media, *Water Resources Research*,  
979 **5**(6), 1273–1289.

- 980 Steelman, C., Parker, B., & Kennedy, C., 2015. Evaluating local-scale anisotropy and het-  
981 erogeneity along a fractured sedimentary bedrock river using EM azimuthal resistivity and  
982 ground-penetrating radar, *Journal of Applied Geophysics*, **116**, 156–166.
- 983 Steinich, B. & Marin, L. E., 1996. Hydrogeological investigations in northwestern Yucatan,  
984 Mexico, using resistivity surveys, *Groundwater*, **34**(4), 640–646.
- 985 Taylor, R. W. & Fleming, A. H., 1988. Characterizing jointed systems by azimuthal resistivity  
986 surveys, *Ground Water*, **26**(4), 464–474.
- 987 Telford, W. M., Geldart, L. P., & Sheriff, R. E., 1990. *Applied Geophysics*, Cambridge  
988 University Press.
- 989 Tsoflias, G. P., Halihan, T., & Sharp, J. M., 2001. Monitoring pumping test response in a  
990 fractured aquifer using ground-penetrating radar, *Water Resources Research*, **37**(5), 1221–  
991 1229.
- 992 Van Sielen, C. D., 2002. Equivalent channel network model for permeability and electrical  
993 conductivity of fracture networks, *Journal of Geophysical Research: Solid Earth*, **107**(B6).
- 994 Vermilye, J. M. & Scholz, C. H., 1995. Relation between vein length and aperture, *Journal*  
995 *of Structural Geology*, **17**(3), 423–434.
- 996 Wang, M. & Kulatilake, P., 2008. Understanding of hydraulic properties from configurations  
997 of stochastically distributed fracture networks, *Hydrological Processes*, **22**(8), 1125–1135.
- 998 Willot, F. & Jeulin, D., 2011. Elastic and electrical behavior of some random multiscale highly-  
999 contrasted composites, *International Journal for Multiscale Computational Engineering*,  
1000 **9**(3).
- 1001 Wishart, D. N., Slater, L. D., & Gates, A. E., 2008. Fracture anisotropy characterization in  
1002 crystalline bedrock using field-scale azimuthal self potential gradient, *Journal of Hydrology*,  
1003 **358**(1), 35–45.
- 1004 Yadav, G. & Singh, S. K., 2007. Integrated resistivity surveys for delineation of fractures  
1005 for ground water exploration in hard rock areas, *Journal of Applied Geophysics*, **62**(3),  
1006 301–312.
- 1007 Yeboah-Forson, A. & Whitman, D., 2014. Electrical resistivity characterization of anisotropy  
1008 in the Biscayne Aquifer, *Groundwater*, **52**(5), 728–736.
- 1009 Zhao, J., Al, T., Chapman, S. W., Parker, B. L., Mishkin, K. R., Cutt, D., & Wilkin, R. T.,  
1010 2017. Determination of Cr(III) solids formed by reduction of Cr(VI) in a contaminated  
1011 fractured bedrock aquifer: Evidence for natural attenuation of Cr(VI), *Chemical Geology*,  
1012 **474**, 1–8.

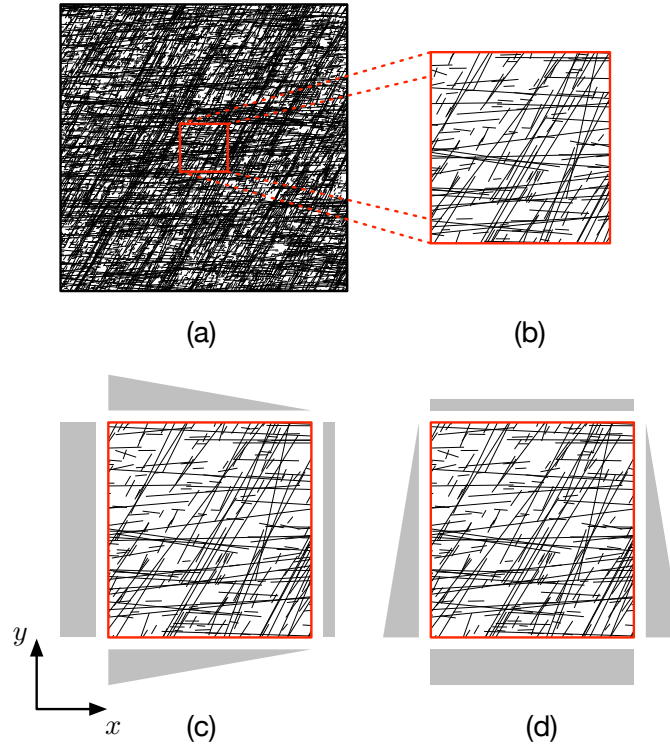


Figure 1: (a) Example discrete fracture network (DFN) generated over a large-scale square domain. (b) Extraction of central square sub-domain upon which fluid- and electric-current-flow simulations are performed. (c) Dirichlet boundary conditions considered for measuring the conductivity tensor components  $C_{xx}$  and  $C_{yx}$ . (d) Dirichlet boundary conditions considered for measuring components  $C_{yy}$  and  $C_{xy}$ .

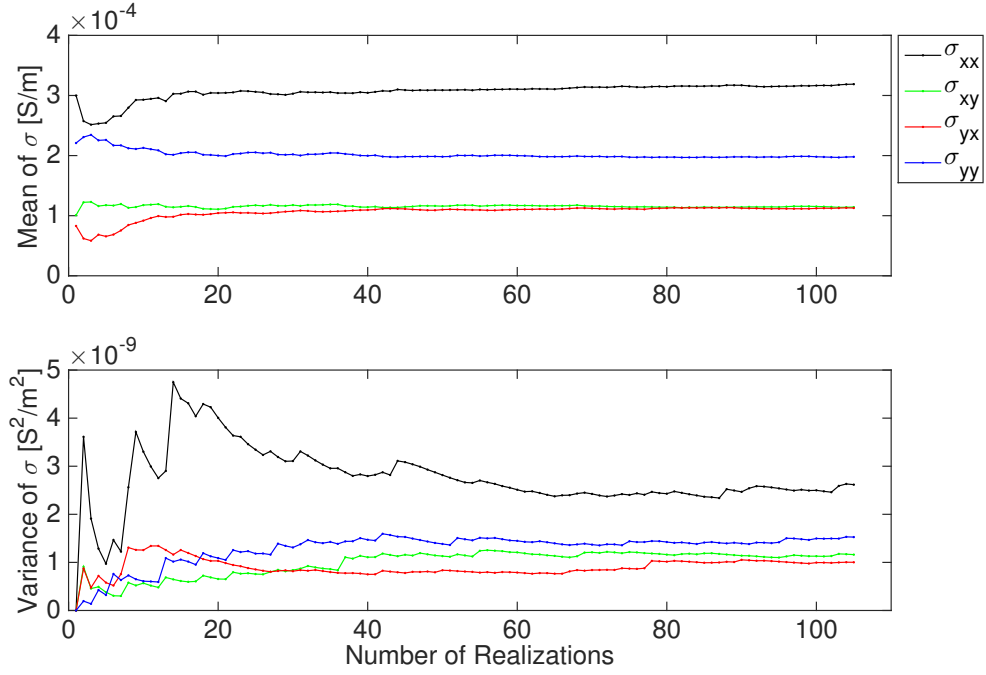


Figure 2: Example showing the calculated mean and variance of the electrical conductivity tensor components  $\sigma_{xx}$ ,  $\sigma_{xy}$ ,  $\sigma_{yx}$ , and  $\sigma_{yy}$ , plotted as a function of the number of considered fracture-network realizations, for a domain size of  $12 \times 12$  m. The presented data correspond to Case 12 from Table 1 with  $\sigma_m/\sigma_f = 10^{-6}$ . See Section 3 for details.

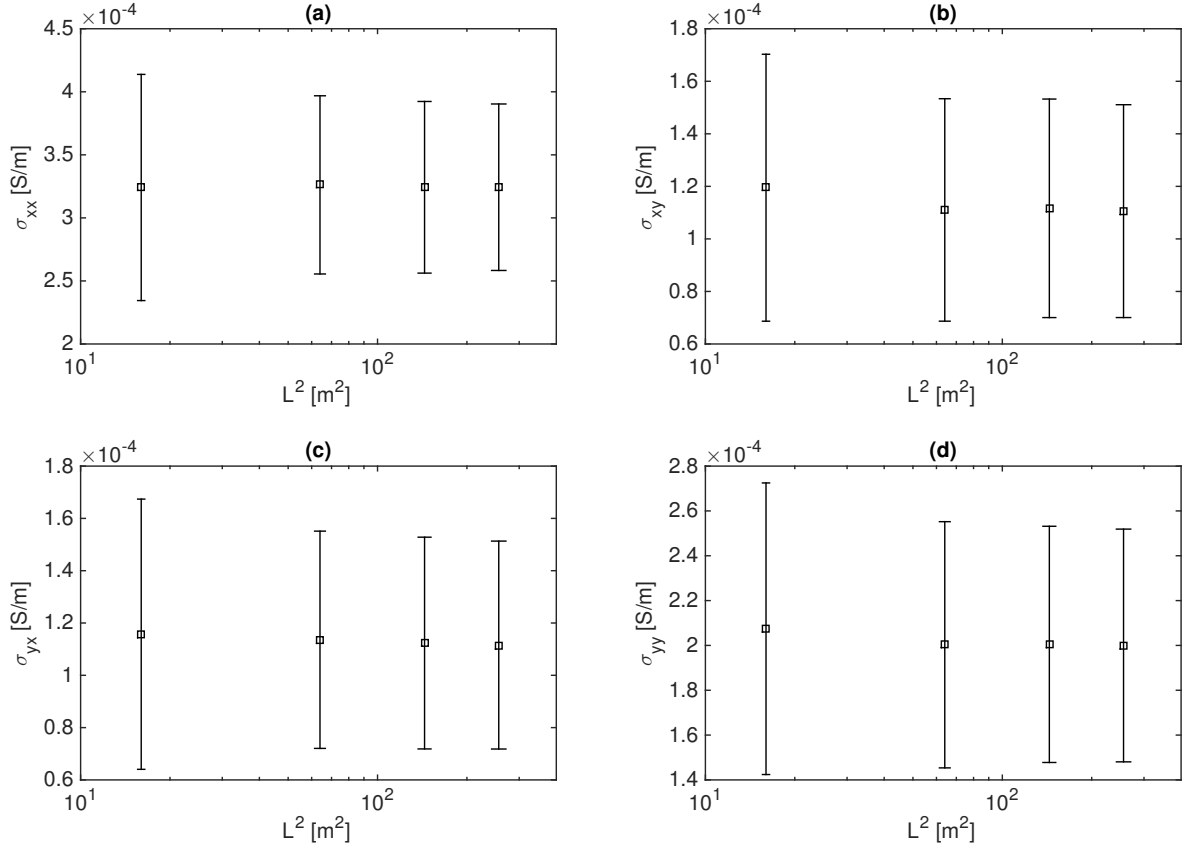


Figure 3: Example showing the stabilized estimates of the mean and standard deviation of the components of the electrical conductivity tensor, plotted as a function of domain area  $L^2$ . The presented data correspond to Case 12 from Table 1 with  $\sigma_m/\sigma_f = 10^{-6}$ . See Section 3 for details.

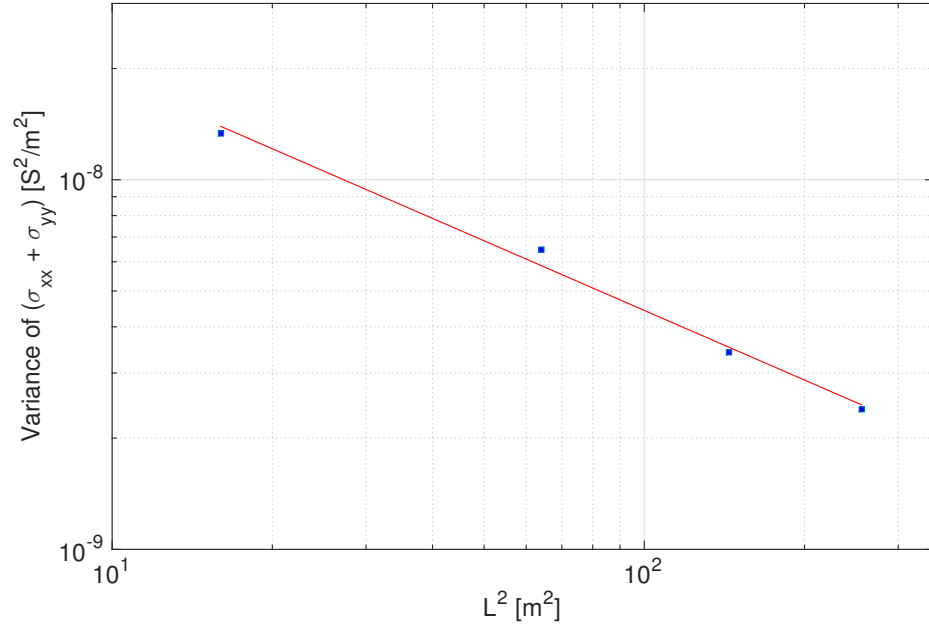


Figure 4: Example showing the variance of  $(\sigma_{xx} + \sigma_{yy})$  plotted as a function of domain area  $L^2$ . The least-squares best-fitting straight line through the points (red) provides the scaling relationship that is used to determine the REV size. The presented data correspond to Case 12 from Table 1 with  $\sigma_m/\sigma_f = 10^{-6}$ . See Section 3 for details.



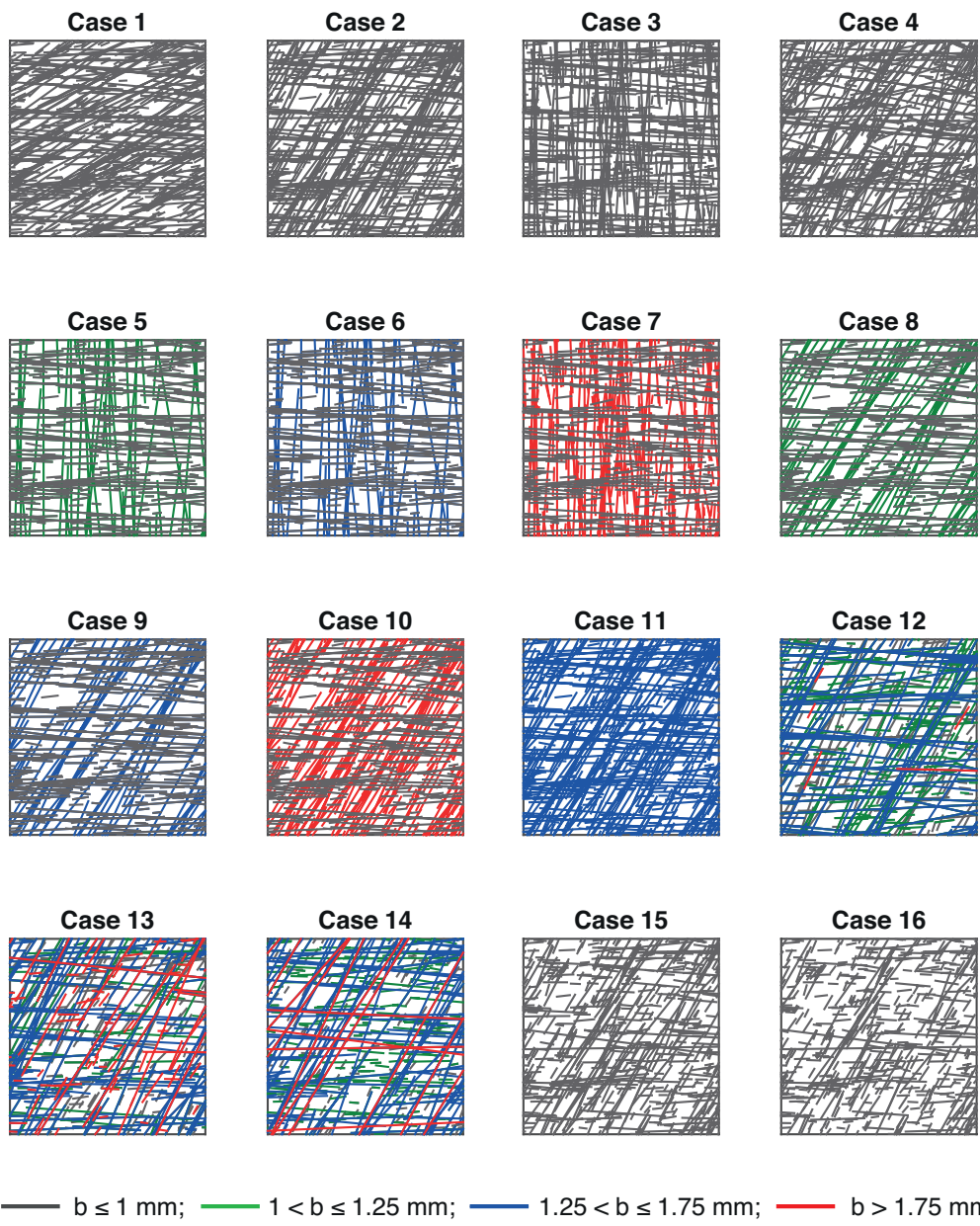


Figure 5: Example discrete fracture networks corresponding to the different test cases described in Table 1. Each square is  $16 \times 16$  m in size.

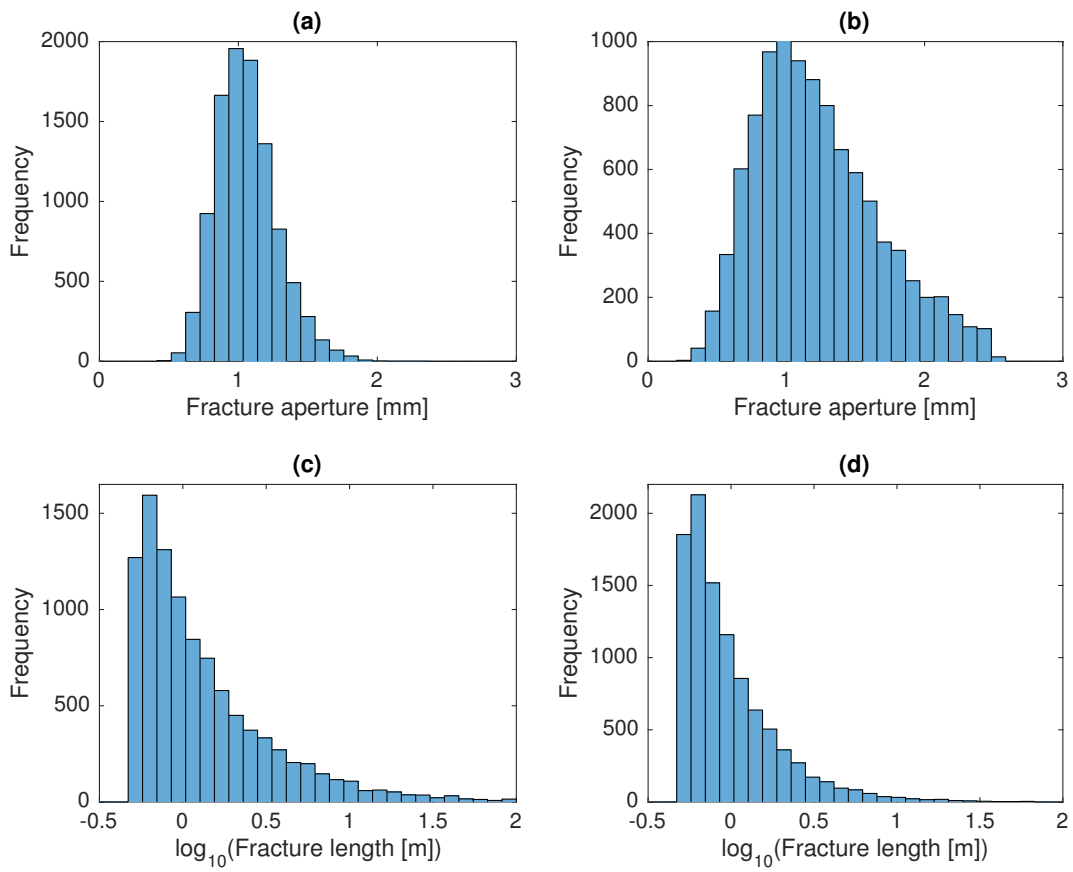


Figure 6: Histograms of the truncated log-normal fracture aperture distribution for (a)  $(\mu_{\ln b}, \sigma_{\ln b}) = (-6.87, 0.2)$ , and (b)  $(\mu_{\ln b}, \sigma_{\ln b}) = (-6.75, 0.4)$ , along with histograms of the truncated power-law fracture length distribution for (c)  $a = 2.0$ , and (d)  $a = 2.5$ .

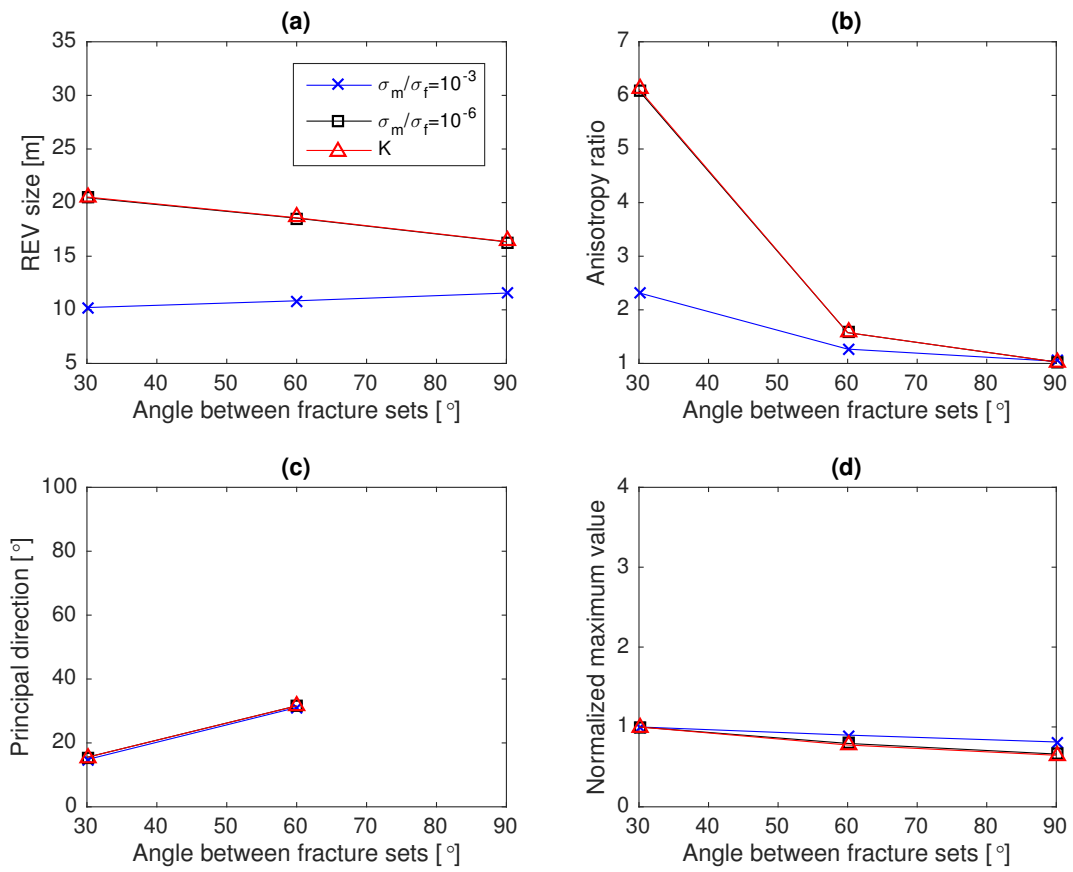


Figure 7: Effect of changing the angle between the two fracture sets on (a) the estimated REV size, (b) the tensor anisotropy ratio, (c) the direction of maximum conductivity; and (d) the maximum conductivity value, normalized between data sets for comparison. Test cases 1, 2, and 3 are considered (Table 1). Note that no principal direction is available when the angle between the fracture sets is  $90^\circ$  because the system is effectively isotropic (Tables 2 and 3).

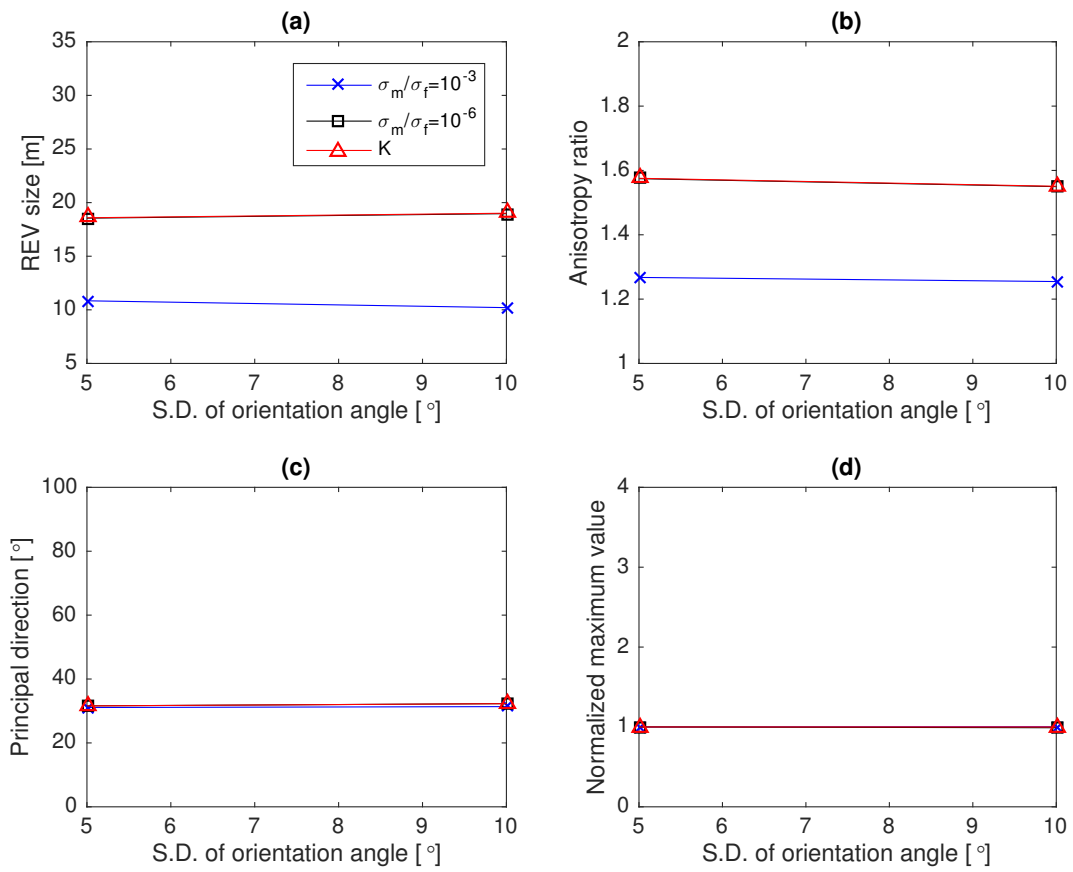


Figure 8: Effect of increasing the standard deviation of the fracture orientation angle on (a) the estimated REV size, (b) the tensor anisotropy ratio, (c) the direction of maximum conductivity; and (d) the maximum conductivity value, normalized between data sets for comparison. Test cases 2 and 4 are considered (Table 1).

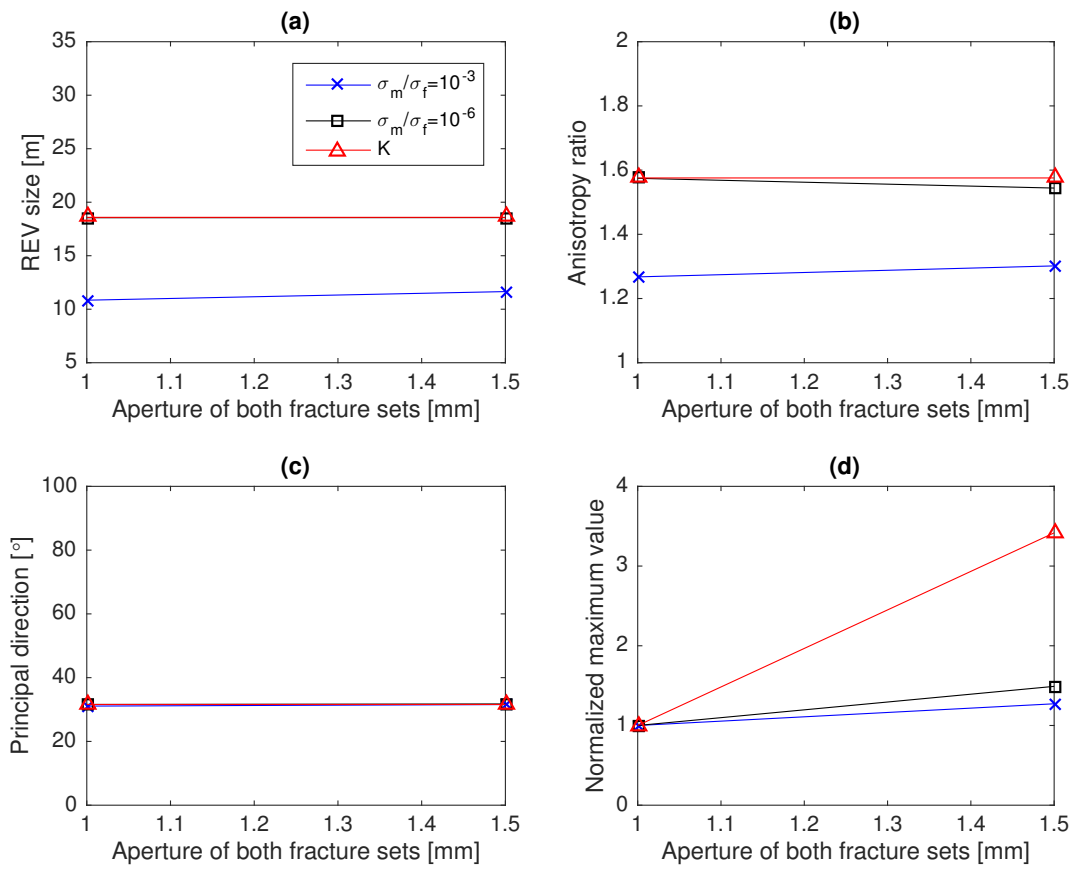


Figure 9: Effect of increasing the aperture of both fracture sets on (a) the estimated REV size, (b) the tensor anisotropy ratio, (c) the direction of maximum conductivity; and (d) the maximum conductivity value, normalized between data sets for comparison. Test cases 2 and 11 are considered (Table 1).

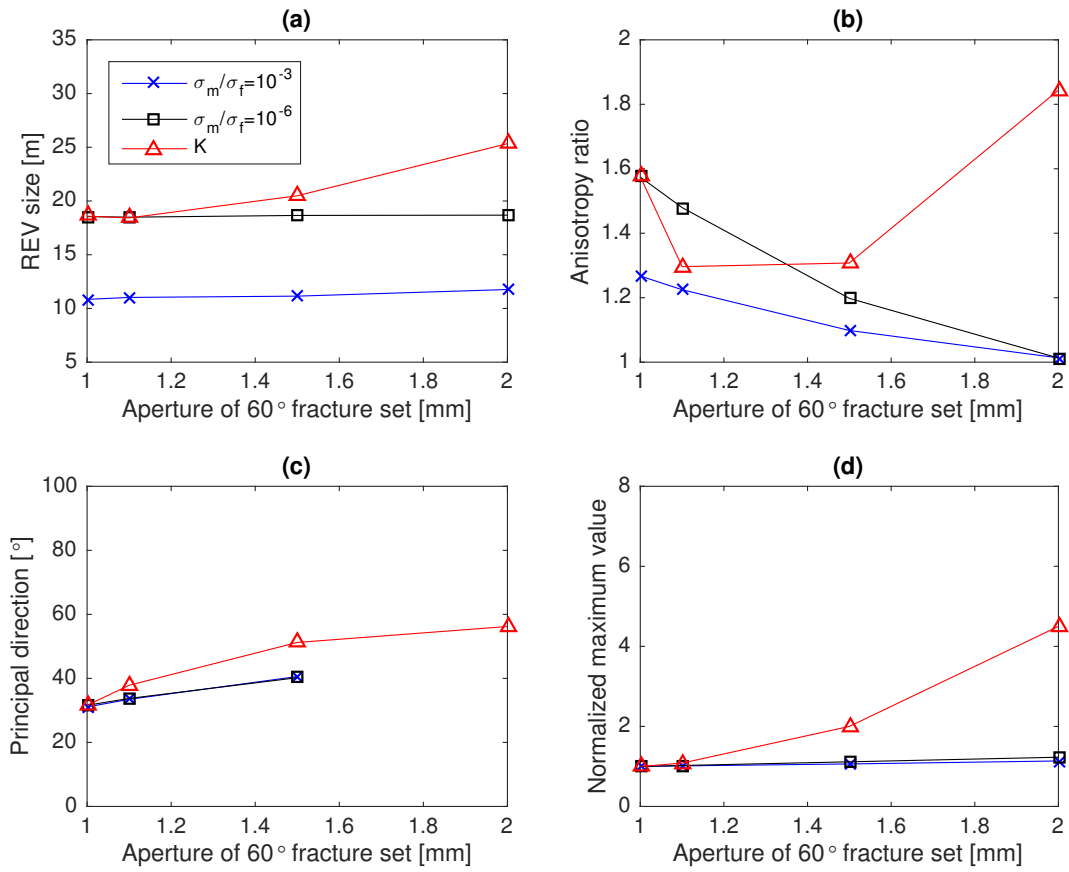


Figure 10: Effect of increasing the aperture of the 60° fracture set on (a) the estimated REV size, (b) the tensor anisotropy ratio, (c) the direction of maximum conductivity; and (d) the maximum conductivity value, normalized between data sets for comparison. Test cases 2, 8, 9, and 10 are considered (Table 1). Note that no principal direction is available for the electrical conductivity when  $b_2 = 2$  mm because the system is effectively isotropic (Tables 2 and 3).

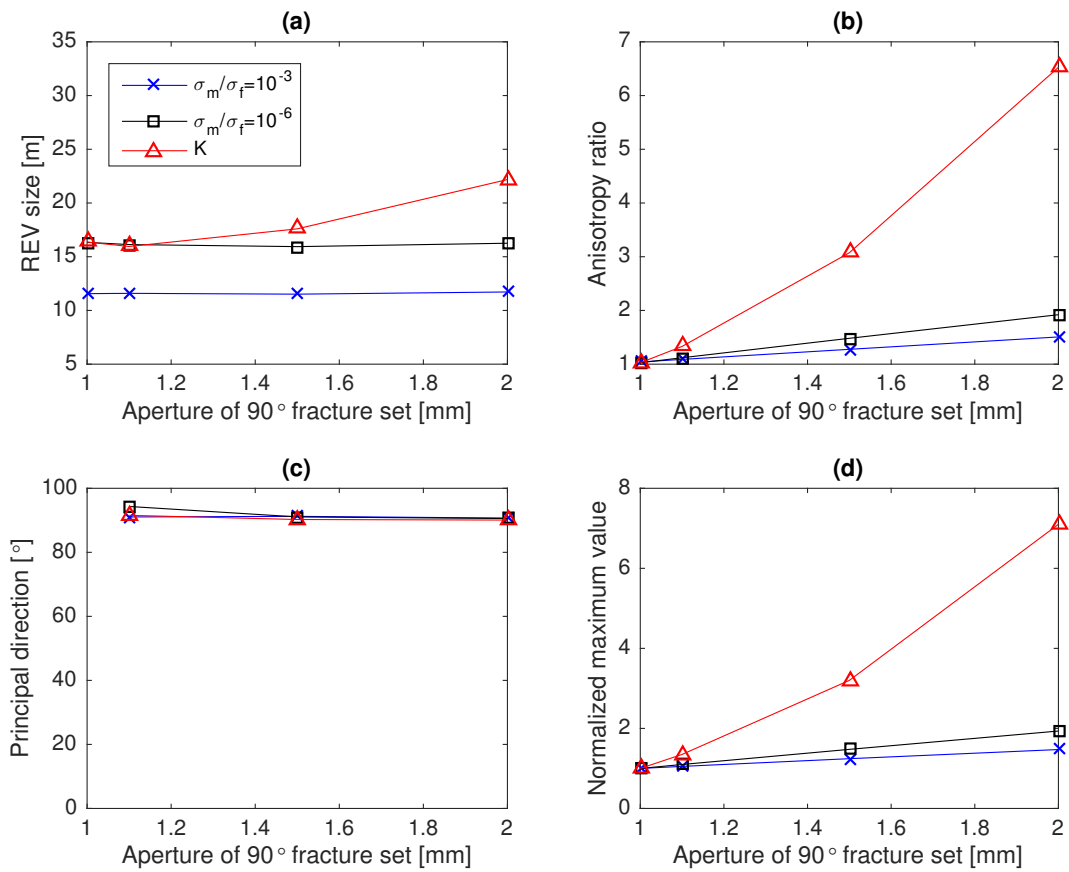


Figure 11: Effect of increasing the aperture of the 90° fracture set on (a) the estimated REV size, (b) the tensor anisotropy ratio, (c) the direction of maximum conductivity; and (d) the maximum conductivity value, normalized between data sets for comparison. Test cases 3, 5, 6, and 7 are considered (Table 1).

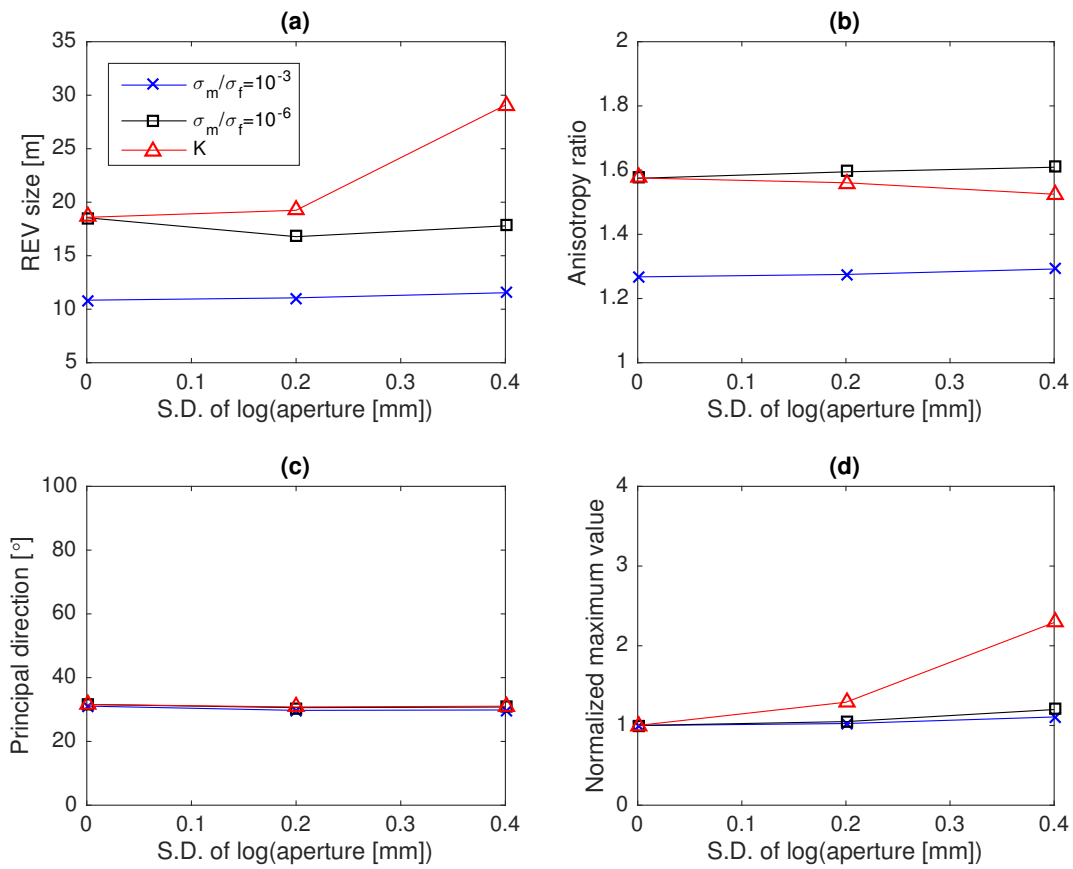


Figure 12: Effect of increasing the fracture-aperture variability on (a) the estimated REV size, (b) the tensor anisotropy ratio, (c) the direction of maximum conductivity; and (d) the maximum conductivity value, normalized between data sets for comparison. Test cases 2, 12, and 13 are considered (Table 1).



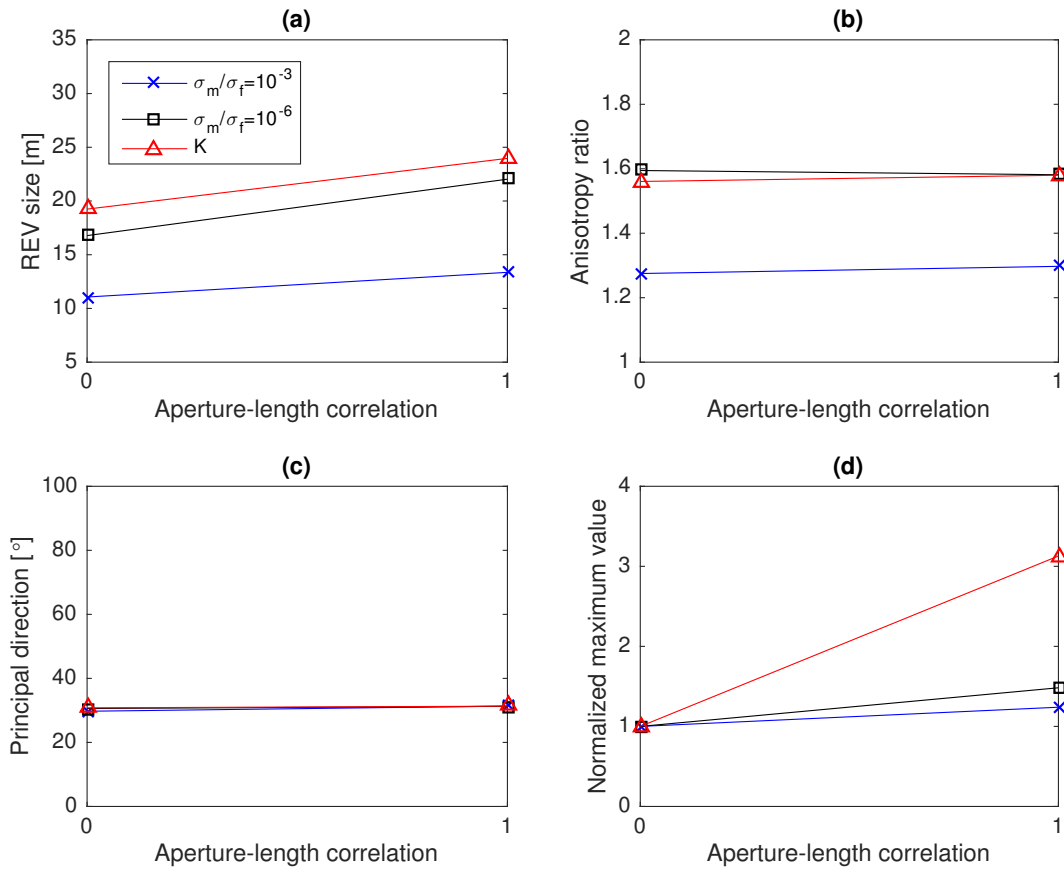


Figure 13: Effect of correlation between aperture and length on (a) the estimated REV size, (b) the tensor anisotropy ratio, (c) the direction of maximum conductivity; and (d) the maximum conductivity value, normalized between data sets for comparison. Test cases 12 and 14 are considered (Table 1). The presence of correlation is indicated on the horizontal axis using a binary variable (0 = uncorrelated; 1 = correlated).

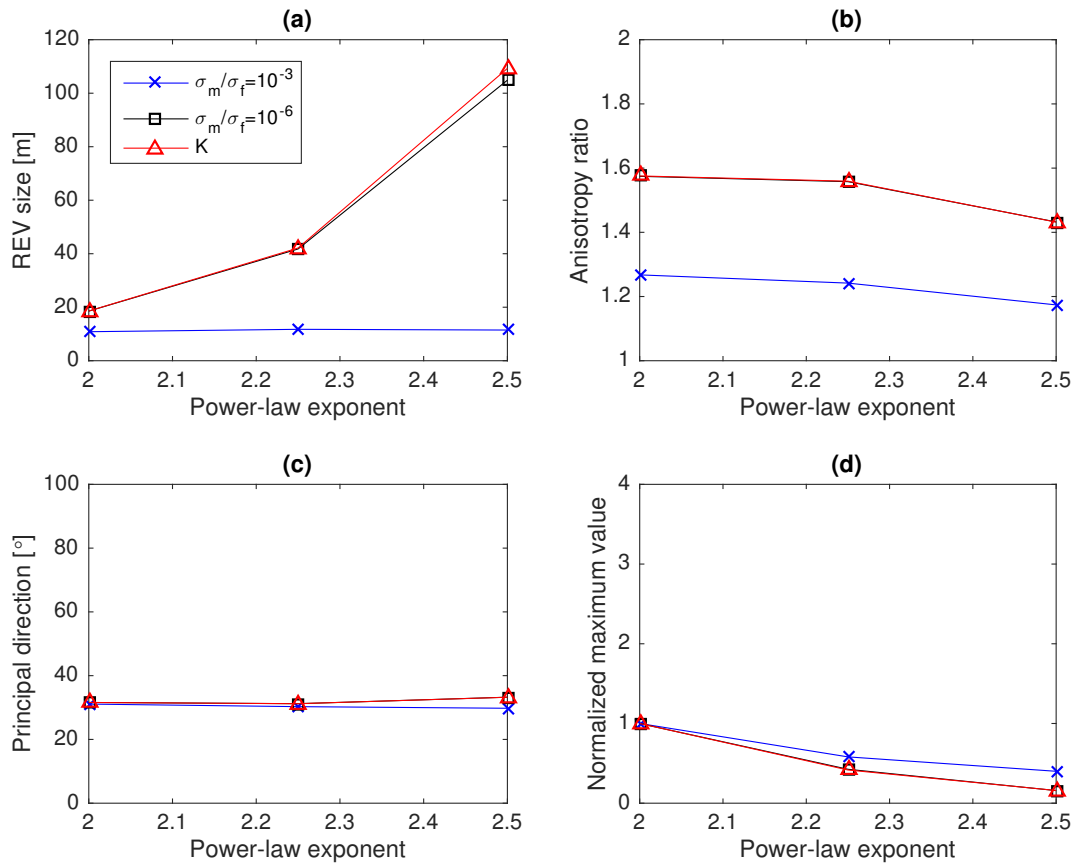


Figure 14: Effect of increasing the fracture-length power-law exponent  $a$  on (a) the estimated REV size, (b) the tensor anisotropy ratio, (c) the direction of maximum conductivity; and (d) the maximum conductivity value, normalized between data sets for comparison. Test cases 2, 15, and 16 are considered (Table 1).

Table 1: Values considered in each test case for the orientation angle ( $\theta$ ), aperture ( $b$ ), and length power-law exponent ( $a$ ) for Fracture Sets 1 and 2.  $N(\mu_\theta, \sigma_\theta)$  refers to a normal distribution having mean orientation  $\mu_\theta$  and standard deviation  $\sigma_\theta$ .  $TLN(\mu_{\ln b}, \sigma_{\ln b})$  refers to a truncated log-normal distribution where  $\mu_{\ln b}$  and  $\sigma_{\ln b}$  are the mean and standard deviation of the natural logarithm of the aperture. The truncation limits for the aperture distribution were set to  $b_{min} = 0.1$  mm and  $b_{max} = 2.5$  mm, whereas the lower limit for the fracture length distribution was set to  $\ell_{min} = 0.5$  m. See Figure 6 for the corresponding histograms. The right-most column indicates whether fracture aperture and length are correlated.

Case	$\theta_1$ [°]	$b_1$ [mm]	$a_1$	$\theta_2$ [°]	$b_2$ [mm]	$a_2$	Correlated?
1	N(0,5)	1.0	2.00	N(30,5)	1.0	2.00	no
2	N(0,5)	1.0	2.00	N(60,5)	1.0	2.00	no
3	N(0,5)	1.0	2.00	N(90,5)	1.0	2.00	no
4	N(0,10)	1.0	2.00	N(60,10)	1.0	2.00	no
5	N(0,5)	1.0	2.00	N(90,5)	1.1	2.00	no
6	N(0,5)	1.0	2.00	N(90,5)	1.5	2.00	no
7	N(0,5)	1.0	2.00	N(90,5)	2.0	2.00	no
8	N(0,5)	1.0	2.00	N(60,5)	1.1	2.00	no
9	N(0,5)	1.0	2.00	N(60,5)	1.5	2.00	no
10	N(0,5)	1.0	2.00	N(60,5)	2.0	2.00	no
11	N(0,5)	1.5	2.00	N(60,5)	1.5	2.00	no
12	N(0,5)	TLN(-6.87,0.2)	2.00	N(60,5)	TLN(-6.87,0.2)	2.00	no
13	N(0,5)	TLN(-6.75,0.4)	2.00	N(60,5)	TLN(-6.75,0.4)	2.00	no
14	N(0,5)	TLN(-6.87,0.2)	2.00	N(60,5)	TLN(-6.87,0.2)	2.00	yes
15	N(0,5)	1.0	2.25	N(60,5)	1.0	2.25	no
16	N(0,5)	1.0	2.50	N(60,5)	1.0	2.50	no

Table 2: Estimated REV size and equivalent tensor characteristics for the electrical conductivity  $\sigma$  when  $\sigma_m/\sigma_f = 10^{-3}$ . Parameters  $\sigma_{max}$  and  $\sigma_{min}$  represent the principal values of the conductivity tensor, whereas  $\theta_p$  is the direction of maximum conductivity. The anisotropy ratio is given by  $\sigma_{max}/\sigma_{min}$ . Note that  $\theta_p$  is shown only for  $\sigma_{max}/\sigma_{min} \geq 1.05$ .

Case	REV size [m]	$\sigma_{max}$ [ $10^{-4}$ S/m]	$\sigma_{min}$ [ $10^{-4}$ S/m]	$\sigma_{max}/\sigma_{min}$	$\theta_p$ [ $^\circ$ ]
1	10.21	6.66	2.88	2.32	14.8
2	10.84	5.98	4.72	1.27	31.1
3	11.56	5.41	5.20	1.04	—
4	10.20	6.00	4.78	1.25	31.4
5	11.59	5.68	5.22	1.09	91.1
6	11.52	6.73	5.27	1.28	91.2
7	11.72	7.96	5.28	1.52	90.7
8	11.03	6.06	4.95	1.22	33.5
9	11.15	6.35	5.78	1.10	40.6
10	11.76	6.80	6.71	1.01	—
11	11.65	7.61	5.85	1.30	31.6
12	11.06	6.13	4.81	1.28	29.7
13	11.54	6.62	5.12	1.29	29.9
14	13.36	7.60	5.86	1.30	31.3
15	11.74	3.48	2.80	1.24	30.3
16	11.47	2.39	2.04	1.17	29.8

Table 3: Estimated REV size and equivalent tensor characteristics for the electrical conductivity  $\sigma$  when  $\sigma_m/\sigma_f = 10^{-6}$ . Parameters  $\sigma_{max}$  and  $\sigma_{min}$  represent the principal values of the conductivity tensor, whereas  $\theta_p$  is the direction of maximum conductivity. The anisotropy ratio is given by  $\sigma_{max}/\sigma_{min}$ . Note that  $\theta_p$  is shown only for  $\sigma_{max}/\sigma_{min} \geq 1.05$ .

Case	REV size [m]	$\sigma_{max}$ [ $10^{-4}$ S/m]	$\sigma_{min}$ [ $10^{-4}$ S/m]	$\sigma_{max}/\sigma_{min}$	$\theta_p$ [°]
1	20.45	3.74	0.62	6.09	15.5
2	18.55	2.97	1.89	1.57	31.6
3	16.34	2.47	2.41	1.03	—
4	18.97	2.94	1.90	1.55	32.3
5	16.13	2.71	2.42	1.12	94.3
6	15.94	3.65	2.46	1.48	91.1
7	16.26	4.78	2.49	1.92	90.6
8	18.50	3.04	2.05	1.48	33.7
9	18.66	3.31	2.76	1.20	40.2
10	18.68	3.65	3.61	1.01	—
11	18.56	4.43	2.87	1.54	31.8
12	16.78	3.11	1.95	1.59	30.6
13	17.79	3.56	2.21	1.61	30.8
14	22.03	4.62	2.92	1.58	31.3
15	41.78	1.26	0.81	1.56	31.2
16	104.87	0.47	0.33	1.43	33.2

Table 4: Estimated REV size and equivalent tensor characteristics for the hydraulic conductivity  $K$ . Parameters  $K_{max}$  and  $K_{min}$  represent the principal values of the conductivity tensor, whereas  $\theta_p$  is the direction of maximum conductivity. The anisotropy ratio is given by  $K_{max}/K_{min}$ . Note that  $\theta_p$  is shown only for  $K_{max}/K_{min} \geq 1.05$ .

Case	REV size [m]	$K_{max}$ [ $10^{-3}$ m/s]	$K_{min}$ [ $10^{-3}$ m/s]	$K_{max}/K_{min}$	$\theta_p$ [ $^\circ$ ]
1	20.52	3.10	0.50	6.12	15.5
2	18.59	2.40	1.50	1.58	31.6
3	16.37	2.00	2.00	1.03	—
4	19.01	2.40	1.50	1.55	32.3
5	15.95	2.70	2.00	1.33	91.6
6	17.59	6.40	2.10	3.07	90.3
7	22.18	14.20	2.20	6.53	90.1
8	18.43	2.60	2.00	1.30	37.8
9	20.49	4.80	3.70	1.31	51.2
10	25.34	10.80	5.90	1.84	56.2
11	18.59	8.20	5.20	1.58	31.6
12	19.25	3.10	2.00	1.56	30.8
13	29.07	5.50	3.60	1.52	31.0
14	23.97	9.70	6.10	1.58	31.3
15	42.13	1.00	0.66	1.56	31.2
16	109.26	0.38	0.27	1.43	33.2